Characterization of apatite within the Mactung W (Cu,Au) skarn deposit, Northwest

Territories: implication for the evolution of skarn fluids

By
Andree Roy-Garand

A Thesis Submitted to
Saint Mary's University, Halifax, Nova Scotia
in Partial Fulfillment of the Requirements for
the Degree of Geology.

November 25th, 2019, Halifax, Nova Scotia

Approved: Erin Adlakha

Approved: Yana Fedortchouk

Date: November 25th, 2019

Characterization of apatite within the Mactung W (Cu,Au) skarn deposit, Northwest

Territories: implication for the evolution of skarn fluids

By: Andree Roy-Garand

Abstract

Skarn-hosted apatite from the Mactung deposit, Selwyn Basin, Northwest Territories, Canada, is characterized to understand the chemical evolution and signatures of mineralizing fluids. Petrography and rare earth element (REE) abundances constrain three generations of fluorapatite, each of which record distinct moments in the system's evolution. *Type-i* apatite occur with detrital phosphate nodules. This apatite contains variable ΣREE+Y (1314 ± 821 ppm, 1σ, n = 78) and show negatively sloping chondrite normalized REE+Y (REE+Y$_N$) patterns with variable LREE$_N$/HREE$_N$ (La$_N$/Lu$_N$ = 27 ± 30) and weak Eu anomalies (Eu$_N$/Eu$_N$* = 0.6 ± 0.2; Eu* = $\sqrt{Sm_N * Gd_N}$). The REE abundances of phosphate nodules from Mactung are similar to those reported in unmineralized units at Howards Pass in the Selwyn Basin. These REE patterns are similar to that of type-i apatite, suggesting that type-i apatite are recrystallization products of phosphate nodules, likely during isochemical contact metamorphism. Hydrothermal *type-ii* apatite occur with skarn assemblages and are divided into two sub-types: i) early type-ii apatite occur in prograde skarns and show high flat lying REE+Y$_N$ patterns (e.g., ΣREE+Y = 17194 ppm, La$_N$/Lu$_N$ = 3.5, n = 31) with negative Eu anomalies (e.g., Eu$_N$/Eu$_N$* = 0.1) and ii) later type-ii apatite occur in retrograde skarns and show bowl shaped to negatively sloped REE+Y$_N$ patterns, reflecting low MREE content (e.g. La$_N$/Sm$_N$ = 10.2, Sm$_N$/Lu$_N$ = 0.3, n = 17), and positive Eu anomalies (e.g., Eu$_N$/Eu$_N$* = 14.3). *Type-iii* apatite are associated with quartz-scheelite veins, which cross-cut prograde skarn. These apatite contain high ΣREE+Y (7752 ± 496 ppm, n = 3) and exhibit bowl-shaped REE+Y$_N$ patterns, corresponding to low MREE (La$_N$/Sm$_N$ = 8 ± 0.3), and no Eu anomaly. The REE patterns and paragenesis of hydrothermal apatite (i.e. type-ii and type-iii) indicate the presence of two chemically distinct ore fluids during the different stages of mineralization of the Mactung deposit. The first fluid is associated with prograde skarns and early type-ii apatite, whereas the second fluid, recorded in late type-ii and type-iii apatite, formed retrograde skarn and quartz veins. The REE+Y$_N$ patterns of late type-ii and type-iii apatite record a MREE fractionation through early crystallization of MREE-rich minerals.

Table of Contents

List of Figures

List of Tables

Introduction

Apatite is a common accessory mineral in all rock types and has the ability to accommodate a wide variety of trace elements and rare earth elements (REE) in its crystal structure (Harlov, 2015). The high apatite-fluid partitioning coefficients for REE and other metals (e.g., Y, Mn, Sr) allows for these elements to be preferentially partitioned into the apatite structure over other co-precipitating minerals (Watson and Ayers, 1993). This property has driven recent interest in the study of apatite as it is suggested that the trace element and REE composition of apatite may reflect the nature of associated hydrothermal fluids. Therefore, apatite has the potential to fingerprint and record the chemical evolution of hydrothermal fluids in ore systems. The applications of apatite to record hydrothermal fluids has been demonstrated in previous studies: i) as an indicator mineral to discriminate ore zones in porphyry-Cu deposits (Bouzari et al., 2016) ii) in modelling ore mineralization associated with multiple chemically distinct fluids in IOCG deposits (Cruz et al., 2019), and iii) in fingerprinting different fluids in hydrothermal skarn deposits (Adlakha et al., 2018). These aforementioned studies demonstrate that fluid evolution in ore systems can be effectively constrained through the categorization of multiple generations of apatite based of petrography and chemical signatures. Specifically, distinct chondrite normalized (CN) REE signatures of different generations of apatite may reflect discrete fluids and their evolution in hydrothermal ore systems

This B.Sc. honours project characterizes multiple generation of skarn hosted apatite from the Mactung W (Cu, Au) skarn deposit. The Mactung deposit outcrops on Mount Allen on the Yukon-Northwest Territories border and hosts one of the world's largest tungsten concentrations with estimated reserves of 17 Mt and total mineral resources grading 0.97 % WO_3 and 0.078% Cu (Dick and Hodgson, 1982). Hydrothermal skarn

mineralization is believed to be related to the intrusion of late Cretaceous felsic plutons that outcrop near the deposit; although, subsequent studies suggest the influence of a blind intrusion at depth (Atkinson and Baker, 1979). The nature of hydrothermal fluids associated with mineralization at Mactung remains poorly constrained. Adlakha et al., (2018) classified multiple generation of skarn hosted apatite from Cantung, a tungsten deposit from the same district as Mactung. The author's revealed that apatite recorded discrete hydrothermal events associated with ore mineralization. Considering the prior success in the application of apatite as a fluid tracer at Cantung, similar methods will be applied to the Mactung deposit in the current study. These include the characterization of different generations of apatite using classic petrographic techniques in conjunction the Scanning Electron Microscope (SEM), Cathodoluminescence (CL) and micro-X-Ray Fluorescence (micro-XRF). The major and trace element (including REE) composition of apatite was quantified with the use of the Electron Probe Micro-Analyser (EPMA) and Laser Ablation Inductively Coupled Plasma Mass Spectrometry (LA-ICP-MS). These results will be used to discriminate the signatures and evolution of mineralizing fluids of the Mactung deposit and, in turn, evaluate the ability of apatite to record discrete mineralizing events in geochemical systems

Background

Apatite Mineral Chemistry

Apatite is a widely occurring calcium phosphate mineral. The low solubility of P_2O_5 in silicate melts and aqueous fluids commonly causes apatite to be paragenetically early, this leads its trace and REE chemistry to be largely unaffected by fractionation of coeval minerals (Webster and Piccoli, 2015). These characteristics allow apatite to record the chemical fluid evolution of geological systems as variations in its trace element chemistry

is a function of pressure, temperature and fluid composition at the time of crystallization (Bouzari et al., 2016).

Apatite is a hexagonal mineral with crystal structure consisting of PO_4^{3-} laterally bonded with Ca^{2+} in hexagonal closest packing (Nesse, 2017). Calcium ions are in two different coordination with 40% of ions occurring in 6-fold coordination (Ca1) and 60% of ions occurring 7-fold coordination (Ca2) with oxygen from the phosphate group and an anionic group (F, OH or Cl) (Nesse, 2017). The crystal structure of apatite and coordination of Ca^{2+} allows it to accommodate large structural distortions enabling the occurrence of a variety of chemical substitutions (Hughes and Rakovan, 2002; Pan and Fleet, 2002). Monovalent ions such as Li^+, Na^+, K^+, Na^+ and Rb^+, can substitute in the Ca1 site; Na^+ is the most common monovalent ion occurring in minor concentrations (Pan and Fleet, 2002). Divalent ion substitution in apatite include Sr^{2+}, Ba^{2+}, Mg^{2+}, Fe^{2+}, Eu^{2+} and Pb^{2+}, which are accommodated in either Ca^{2+} site due to their similar charge and size (Rakovan and Hughes, 2000; Pan and Fleet, 2002). Trivalent cations substitutions in apatite are REE^{+3} and Y^{+3}, these cations substitute into the Ca1. The substitution of monovalent, divalent and trivalent ions are accommodated through coupled substitutions in order to maintain a charge balance. These ions commonly substitute with SiO_4^{4-}, SO_4^{2-}, AsO_4^{3-} and V_2O^+, which occupy the PO_4^{3-} site (Hughes and Rakovan, 2015). Tetravalent ions U^{4+} and Th^{4+} can substitute in either Ca^{2+} sites along with a vacancy to accommodate the charge balance (Fleet & Pan, 2002). Anionic substitution occurs between F, Cl and OH. The concentration of these anions define the three endmembers of the apatite supergroup: fluorapatite (F), chlorapatite (Cl) and hydroxylapatite (OH) (Hughes and Rakovan, 2015).

Rare earth elements are trivalent cations that form the lanthanide series; these elements are commonly grouped with Y due to their similar chemical properties and

behavior in geochemical systems. Apatite has the capacity to accommodate high concentrations of REE+Y (up to 20%) due to its high mineral-liquid partitioning coefficient (Hughes and Rakovan, 2015). The substitution of REE in apatite occurs in either Ca sites through the following exchange vectors: $(REE+Y)^{3+} + SiO^{4-} = Ca^{2+} + PO^{3-}$, $Na^+ + (REE+Y)^{3+} = 2Ca+$ and $3Ca = 2(REE+Y)^{3+} + vacancy$ (Hughes and Rakovan, 2015). Apatite is one of the few minerals that readily partitions REE, thus its REE chemistry is believed to largely reflect that of its mineralizing fluid (Fleet and Pan, 1995). The fractionation of REE+Y is largely affected by the decrease in ionic radius from La to Lu as well as the multiple oxidation states of Ce and Eu: Ce^{4+} and Eu^{2+} (Lipin and McKay, 1989). Anomalous concentrations of Ce^{4+} and Eu^{2+} relative to the trivalent REE occur as these ions have different chemical properties than trivalent REEs. This information may provide insight on redox conditions of the system at the time of crystallization (Lipin and McKay, 1989). Analyses of the partitioning of REE+Y between apatite and silicate melts indicate that apatite preferentially incorporate MREE relative to LREE and HREE (Watson and Green, 1981). Additionally, Eu^{2+} is less compatible than the other $REE+Y^{3+}$ due to its large ionic radius. Therefore, magmatic apatite commonly shows a convex up CN pattern coupled with a negative europium anomaly (Watson and Green, 1981; Rimstidt et al., 1998). However, in aqueous systems the apatite liquid partitioning coefficient for MREE are less than LREE (Ayers and Watson, 1993). Prior studies regarding apatite liquid partition of REE have additionally demonstrated that Eu^{2+} behaves similarly to $REE+Y^{3+}$. Hence, the negative Eu anomalies in hydrothermal apatite are inherited from the fluid rather than apatite partitioning (Ayers and Watson, 1993).

Skarn Deposits

Skarns are calc-silicate rocks produced through metamorphic and metasomatic reactions by nearby intrusions (Meinart, 1992). The intrusion of a neighboring pluton induces thermal metamorphism and metasomatism which causes ionic exchange at the contacts of contrasting lithologies, the recrystallization of porous rocks (e.g. limestone), and the fracturing of non-porous rocks (Dawson, 1996). The intrusion of metasomatic fluids replaces the mineralogy of the host rock and produces an alteration assemblage of coarse-grained Ca or Mg silicate gangue referred to as a skarn assemblage (Meinart, 1992). Skarn assemblages are subdivided into two types: prograde skarns and retrograde skarns. Prograde skarns are paragenetically early and consist of anhydrous mineral assemblages (e.g., clinopyroxene and garnet) that crystallize at high temperatures. In comparison, retrograde skarns are paragenetically late and comprise hydrous mineral assemblages (e.g., amphibole) at low temperature (Meinart, 1992). Metals such as Fe, W, Au, Cu, Zn, Mo and Sn may occur in skarn in economically viable concentrations (Dawson, 1996). Major economic deposits are found in calcareous strata and are classified into one of five major classes based on the dominant economic mineral occurrence (i.e. Fe, W, Cu, Zn-Pb, Sn) (Einaudi and Burt, 1982).

In tungsten skarns deposits the economically viable concentrations of W are hosted in scheelite (Dawson, 1996). In addition to scheelite, minor concentration of molybdenite, pyrrhotite and chalcopyrite commonly occur (Dawson, 1996). Prograde skarn assemblages of tungsten skarns consist of anhydrous phases such as pyroxene, garnet, calcite, dolomite, quartz, vesuvianite and wollastonite. Conversely retrograde skarn assemblages comprise hydrous phases such as hornblende, biotite, plagioclase, epidote, titanite, chlorite, actinolite

and apatite. Tungsten skarns are commonly associated with felsic calk-alkaline plutons which provide the metal sources for skarns (Dawson, 1996). Tungsten skarns are further subdivided into reduced and oxidized types based on variations in host rock composition, skarn mineralogy and depth (Einaudi and Burt, 1982; Meinart, 1992). Oxidized tungsten skarns form near surface and comprise a mineralogy of andraditic garnet with diopsidic pyroxene. Sulphides are present as pyrite instead of pyrrhotite, ferric iron phases are more common than ferrous phases and scheelite is Mo-poor. Reduced tungsten skarns, such as the Mactung deposit, occur at greater depths and are characterized by a Fe and Ca rich mineral assemblage comprised of hedenbergite pyroxene and grossularite garnet with amphibole, biotite, pyrrhotite and chalcopyrite. Scheelite occurs in two generation as it initially forms early fine-grained Mo-rich scheelite, which is later redeposited in late quartz veins as coarse-grained low Mo-scheelite (Einaudi and Burt, 1982). The Mactung deposit is characterized as a reduced tungsten skarn based on its Fe-rich mineralogy, abundant pyrrhotite mineralization, and presence of methane in fluid inclusions (Dick and Hodgson, 1982; Gretsner, 1989).

Geological considerations

The host rocks of the Mactung deposit occur along the eastern margin of the Cambrian to Devonian Selwyn Basin near its contact with the Mackenzie Carbonate platform. The Selwyn Basin developed in the Neoproterozoic to early Devonian when crustal extension generated the fragmentation of Rodinia, subsequently forming the epicratonic basin (Eisbacher, 1981). Strata of the Selwyn Basin represent a succession of rift and basinal facies bounded by two carbonate platforms: the Mackenzie platform which occurs to the east and the Macdonald platform found in the north.

The oldest stratigraphic unit of the basin is represented by Cambrian conglomeratic rocks deposited as rifting eroded adjacent basement strata. Up stratigraphy lithologies transition into the Cambrian to Ordovician deep water carbonate, which are overlain by chert and pelitic rocks (Eisbacher, 1981). Mafic volcanics are a minor component, occurring as isolated discontinuous flows, dykes and tuff intercalated with basinal facies (Eisbacher, 1981).

Deformation of the Selwyn Basin occurred as late Jurassic convergence initiated folding, developing a northwest trending thin skinned thrust sheet (Baker and Lang, 2001). Such collisional processes likely generated mid-Cretaceous magmatism, which was emplaced a series of granitic plutons in the deformed basin strata now preserved as the 700 km north-west trending Tombstone-Tungsten magmatic belt (Baker and Lang 2001). Geochemical and isotopic evidence suggest this magmatism to be derived from the partial melting of continental crust during subduction related closing of the Selwyn basin (Mair et al., 2006). The entire magmatic belt is characterized by anomalously high concentration of various ore metals (Au, As, Sb, Bi, Te, W, Mo, Ag, Pb and Zn) with emplaced plutons generating the mineralization of various ore occurrences in the region including W-Cu (Zn), Zn (Pb, W) and W (Mo) (Baker and Lang, 2001).

Mactung is a major tungsten skarn deposit is a member of a larger district of tungsten skarn deposits, which are spatially associated with Tungsten plutonic suite (Baker and Lang, 2001). The Mactung deposit is associated with two exposed biotite quartz monzonite stocks; the Cirque Lake stock located to the east. The exposed Cirque lake stock was initially believed to have sourced skarn fluids and metals. However, the study of stockwork veins by Atkinson and Baker (1986) as well as Re-Os and U-Pb geochronology by Selby et al. (2003) suggest that the exposed stock did not source ore-fluids. It is proposed

that the Mactung is only coincidentally located near the Cirque Lake stock. Instead, ore fluids were likely sourced from a blind intrusion to the south of, and below, the deposit (Atkinson and Baker, 1986; Shelby et al., 2003)

Locally, the strata that host the Mactung deposit are overturned, east-west striking pelitic to carbonaceous sedimentary units cut by high angle faults (Atkinson and Baker, 1986). Ore bearing calc-silicate skarn mineralization is hosted within two carbonaceous sequences named the upper (stratigraphic Units 3D, 3E, 3F) and lower (Unit 2B) ore zones, which are separated by the pelitic hornfels of Unit 3C (Figure 1). Unit 1 is the lowest stratigraphic unit comprising early Cambrian clastics and phyllites. Unit 2B overlies Unit 1, the stratigraphic unit represents the lower ore zone as ore mineralization in a massive lens of brecciated limestone bounded by calcareous pelites. This unit was deposited as debris fans. Clasts primarily consist of limestone fragments with lesser phosphate nodules, siliclastics and fossiliferous limestone fragments. Unit 2B gradationally transitions to the overlying Unit 3D. It is dominated by carbonaceous and pyritic fine-grained hornfels intercalated with intraformational conglomerates that contain clasts of mudstone, siltstone, shale and limestone. Unit 3C is conformably overlain by Unit 3D, a layer of thick-bedded phosphatic limestone slump breccias intercalated with pelites. Breccia layers consist of well-sorted clasts of black phosphatic nodules, limestone and siliclastics. Unit 3D gradationally transitions into Unit 3E, where slump breccias thin and become dominantly pelitic. Unit 3E is comprised of intercalated black and brown mudstone, shale, and siltstone with limestone. The overlying Unit 3F consists of interbedded mudstone, shale and limestone (Atkinson and Baker, 1986).

Contact metamorphism and the infiltration of hydrothermal fluids lead to extensive skarn replacement of calcareous strata forming the Mactung deposit (Atkinson and Baker,

1986). These alteration assemblages are commonly categorized into skarn types which share similar mineralogy and petrography. The classification of skarn types describes the degree and nature of alteration undergone by the host rock during metasomatism. Prograde skarns form at higher temperature leading alteration assemblages to be dominated by anhydrous minerals such as wollastonite, garnet and pyroxene. Retrograde skarns form through the low temperature replacement of prograde assemblages. During retrograde alteration, anhydrous mineral phases are replaced by hydrous phases such as amphibole and biotite. Mineralization of scheelite and sulphides also occurs during retrograde alteration. The classification of skarn assemblages is largely descriptive and is subjective to the author's observation. Therefore, discrepancies exist between different studies. Skarn types hosted in the Mactung deposit were previously described by Dick and Hodgson (1982) as well as Atkinson and Baker (1986). Both studies describe skarn assemblages observed in the upper and lower ore zones of the Mactung deposit. In their study Dick and Hodgson (1982) classify five different skarns (wollastonite, garnet-pyroxene, pyroxene-pyrrhotite, amphibole and biotite skarn) while Atkinson and Baker (1986) classify six different skarns (garnet, garnet-pyroxene, pyroxene, pyroxene-pyrrhotite, biotite and quartz skarn). The different classification of skarns in these two studies can be attributed to different subdivisions of skarn assemblages or the exclusion of rare skarn facies by these authors.

Wollastonite skarn is the lowest grade alterations facies described by Dick and Hodgson (1982). This skarn primarily occurs in the outer zones of the deposits and is comprised of fine-grained wollastonite, with lesser garnet, vesuvianite and pyroxene; scheelite and sulfides are absent. Conversely garnet skarn is the lowest grade alteration facies described by Atkinson and Baker (1986). This rare skarn occurs in the outer limits

of the deposit as garnet pods and veins hosted in bleached limestone. Garnet is occasionally intergrown with quartz and trace scheelite (Atkinson and Baker, 1986).

Garnet-Pyroxene skarn is a widespread alteration facies classified in both studies. Garnet and pyroxene are the dominant mineral phases, these are associated with trace remnant calcite, quartz and vesuvianite; pyrrhotite and scheelite are rare (Dick and Hodgson, 1982; Atkinson and Baker, 1986).

Pyroxene-pyrrhotite skarn classified by Dick and Hodgson (1982) describes all skarn assemblages which contain pyroxenes as the dominant silicate mineral and variable pyrrhotite content (up to 80 modal %). Conversely Atkinson and Baker (1986) subdivide this skarn type into: i) pyroxene skarn assemblages which contain less than 7 modal % pyrrhotite and ii) pyroxene-pyrrhotite skarn assemblages which contain greater than 15 modal % pyrrhotite. Associated mineral phases described in both studies include quartz, plagioclase and clinozoisite. Scheelite abundance increases and grain size decreases as pyrrhotite content increases (Dick and Hodgson, 1982; Atkinson and Baker, 1986).

Amphibole skarn is a rare skarn type only classified by Dick and Hodgson (1982). Amphibole alteration in the Mactung deposit initially occurs through the partial replacements of clinopyroxene. Eventually, retrograde alteration forms coarse grained amphibole through the complete replacement of pyroxenes. These coarse grained amphiboles are subsequently subject to replacement by biotite. Dick and Hodgson (1982) characterize amphibole skarns as mineral assemblages which host coarse-grained amphibole, amphiboles rarely occur without pyroxene or biotite. The lack of megascopic amphibole or its frequent association with pyroxenes and biotite likely influenced Atkinson and Baker (1986) to disregard this skarn classification categorizing these alteration assemblages as either pyroxene-pyrrhotite or biotite skarns.

Biotite skarns are high grade alteration facies classified by both Atkinson and Baker (1986) and Dick and Hodgson (1982). Biotite skarns are dominantly hosted in the lower ore zone, fine to coarse grained biotite occur with pyrrhotite, quartz and scheelite with trace amphibole and pyroxene. Scheelite is abundant commonly forming fine-grained aggregates with a corroded appearance decreases (Dick and Hodgson, 1982; Atkinson and Baker, 1986).

Quartz skarns is a rare skarn type only classified by Atkinson and Baker (1986). These skarns form from the flooding of fluids from adjacent quartz veins and host exceptionally large euhedral scheelite with WO_3 grades > 5 wt % (Atkinson and Baker, 1986). Although Dick and Hodgson (1982) do not classify this distinct skarn facies, the researchers do discuss the occurrence quartz rich portions of skarn which host high grade scheelite likely analogous with quartz skarns. Skarn assemblages and classifications relevant to this study will be discussed in the sampling section.
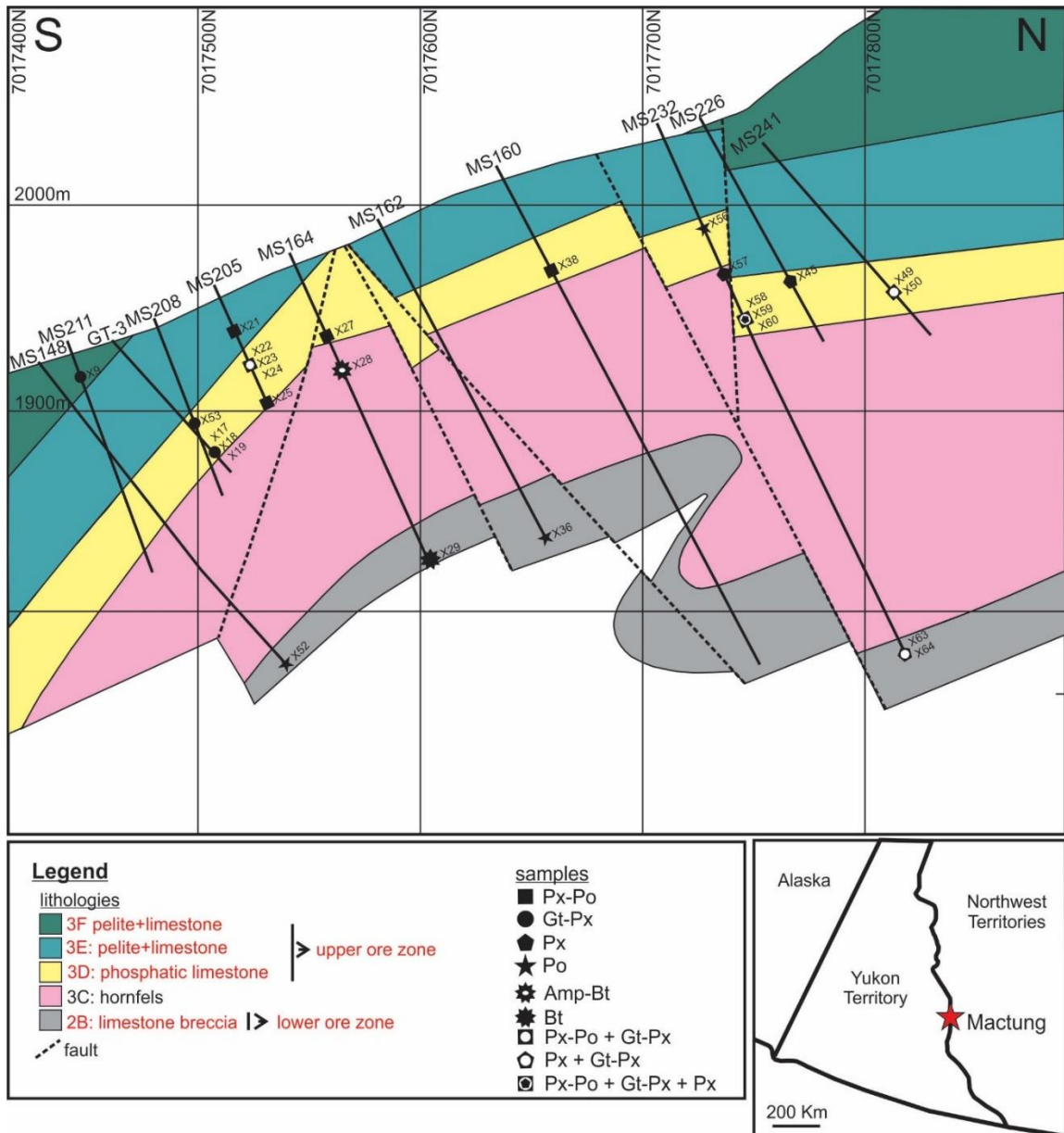
Figure 1: North-south cross section of the Mactung deposit showing the stratigraphy, drillhole location, and location of selected apatite bearing samples. Sample symbols on map indicate skarn type. Modified from Nacisco (2009). Px-Po: pyroxene-pyrrhotite skarn, Gt-Px: garnet-pyroxene skarn, Px: pyroxene skarn, Po: pyrrhotite skarn, Amp-Bt: amphibole-biotite Bt: biotite skarn

Sampling

Fieldwork was conducted by Dr. Erin Adlakha in August 2016. The main drillholes sampled occur along Line 212 of the local map grid, which runs north-south and bisects the Mactung deposit in the western part of the property (Figure 1). This line was selected as drillcores intersect the top-most unit of the upper ore zone (3F). To the east, drillholes only intersect the lower units; although, a few of these were also sampled for comparison. The results of this fieldwork indicate that the skarn units of Mactung are dominated by pyroxene ± pyrrhotite skarn in the lower ore zone, and pyroxene ± pyrrhotite ± garnet skarn in the upper zone. Amphibole and biotite skarns are rare and only occur in the 3C hornfels and the lower ore zone. Representative samples of skarn in the different ore horizons were collected (Figure 1) although, the samples were dominated by pyroxene-pyrrhotite skarn.

Sixty-six thin sections were produced and analysed for apatite using transmitted and reflected light microscopy. Twenty-nine samples bearing apatite and/or phosphate nodules were selected for complete petrographic study by transmitted and reflected light microscopy, as well as scanning electron microscope (SEM). The mineral assemblages of the 29 apatite bearing samples were characterized into six skarn types; wollastonite, garnet-pyroxene, pyroxene, pyroxene-pyrrhotite, pyrrhotite, amphibole-biotite and biotite (Table 1). Some skarn are crosscut by late quartz veins. Petrographic observation of wollastonite, garnet-pyroxene, pyroxene-pyrrhotite, amphibole-biotite and biotite closely resembled those described by Atkinson and Baker (1986), as well as Dick and Hodgson (1982). Pyrrhotite skarn was classified as a separate skarn type in this study but appears to have been grouped with pyroxene-pyrrhotite skarn in these prior studies. The quartz skarn described by Atkinson and Baker (1986) is likely equivalent to the crosscutting quartz veins

observed in this study. The complete descriptions of skarn assemblages can be found in the *Skarn petrography* section of the appendix. Eleven representative samples were selected for apatite mineral chemistry characterization based on apatite quality and petrographic results in order to represent each stratigraphic unit and skarn type (Table 1). The following samples were selected: one garnet-pyroxene skarn sample (X9) from the 3F pelitic limestone, one pyroxene-pyrrhotite skarn sample (X21) from 3E pelitic limestone, three pyroxene-pyrrhotite skarn samples (X49, X38, X27) from 3D phosphatic limestone, one pyroxene skarn sample (X59) from 3D phosphatic limestone, one garnet-pyroxene skarn sample (X53) from 3D limestone, one pyroxene-pyrrhotite (X25) and one amphibole-biotite (X28) from 3C hornfels, two pyrrhotite (X52, X36) skarn sample from 2B phosphatic limestone and one pyroxene skarn sample (X63) from 2B limestone.

Table 1: Drill-hole number (DDH), depth, lithology and skarn type of apatite bearing samples, as well as analytical methods conducted on selected samples

sample	DDH	depth	lithology	unit	skarn*	conducted analyses
x2	MT-80-133	80	limestone	3F	Wo	
x9	MS211	15.75	hornfels	3F	Grt-Cpx	Cl, EPMA, LA-ICP-MS
x17	MS208	77	limestone	3D	Grt-Cpx	
x18	MS208	81	limestone	3D	Wo	
x19	MS208	81.9	hornfels	3C-3D	Grt-Cpx	
x21	MS205	28.75	hornfels	3E	Cpx-Po	Cl, EPMA, LA-ICP-MS, XRF
x22	MS205	62.9	limestone	3D	Grt-Cpx	
x23	MS205	64.6	limestone	3D	Cpx-Po	
x24	MS205	71.5	hornfels	3D	Cpx-Po	
X25	MS205	79.4	hornfels	3C	Cpx-po	Cl, EPMA, LA-ICP-MS, XRF
x27	MS164	59.9	hornfels	3D	Cpx-Po	Cl, EPMA, LA-ICP-MS
x28	MS164	75.2	hornfels	3C	Amp-Bt	Cl, EPMA, LA-ICP-MS
x29	MS164	176.5	hornfels	2B	Bt	
x36	MS162	164.4	limestone	2B	Po	Cl, EPMA, LA-ICP-MS
x38	MS160	49.2	hornfels	3D	Cpx-Po	Cl, EPMA, LA-ICP-MS
x40	MS160	178.4	limestone	2B	Wo	
x45	MS226	52.9	hornfels	3D	Cpx	
x46	MS226	72.9	hornfels	3C	Amp	
x49	MS241	110.2	hornfels	3D	Cpx-Po	Cl, EPMA, LA-ICP-MS
x50	MS241	111.7	hornfels	3D	Grt-Cpx	
x52	MS148	297	limestone	2B	Po	Cl, EPMA, LA-ICP-MS
x53	GT-3	48.2	limestone/hornfels	3D	Grt-Cpx	Cl, EPMA, LA-ICP-MS
x56	MS232	24.55	limestone	3D	Po	
x57	MS232	40.4	hornfels	3C	Cpx	
x58	MS232	54	hornfels	3D	Grt-Cpx	
x59	MS232	56.6	hornfels	3D	Cpx	Cl, EPMA, LA-ICP-MS
x60	MS232	57.4	hornfels	3D	Cpx-Po	
x63	MS232	246.6	hornfels	2B	Cpx	Cl, EPMA, LA-ICP-MS
x64	MS232	246.8	hornfels	2B	Grt-Cpx	

*Amp-Bt=amphibole-biotite, Bt=Biotite, Cpx=pyroxene, Cpx-Po=pyroxene-pyrrhotite, Grt-Cpx=garnet-pyroxene, Po=pyrrhotite, Wo=Wollastonite

Methods

Mineral identification and textural analysis were conducted on the 29-apatite bearing polished thin sections (~30 µm) using the petrographic microscope in both transmitted and reflected light. Petrographic reports were created for all sections recording mineral modal abundance, textural relationships and apatite characteristics (appendix). Based on this information mineral assemblage and paragenesis were interpreted, and skarn types were classified (Table 1). Detailed textural analyses and mineral identification of selected samples was complete using back scattered electron imaging (BSE) and energy dispersive x-ray spectroscopy (EDS) on carbon-coated thin sections using a TESCAN MIRA 3LMU Variable-Pressure Schottky Field-Emission Scanning Electron Microscope (SEM) at Saint Mary's University, Halifax, Nova Scotia. Sample were analyzed set at a working distance of 17 mm with a voltage of 20 kV and a EDS data collection time of 30s/spot. Quantification of major oxides was done using EDS data and the INCA software.

Hot Cathodoluminescence (HCL) was conducted on 11 samples (Table 1) to characterize apatite based on internal luminescence colour and zoning pattern. Imaging was conducted using the Lumic HC4-LM hot-cathode cathodoluminescence microscope coupled with the Olympus BXFM focusing mount at Saint Mary's University. Imaging was conducted using a Kappa DX40C Peltier-cooled camera and DX40C-285FW software. Carbon coated thin sections were analyzed at an acceleration voltage ranging between 10 and 14 kV, beam voltage of 0.24 mA, filament current of 1.8 A, deflection of 7V and a focus of 6V.

Major and minor elements of apatite from six thin sections were quantified by electron probe micro-analyzer (EPMA) using wavelength dispersive spectroscopy (Table

1). Analyses were conducted using the JEOL 8230 super probe from the University of Toronto. Selected elements (Cl, Ca, F, Na, Si, Ce, La, Mn, Y, P, Sr) were quantified at an accelerating voltage of 15 kV with a beam size of 10 µm and a beam current of 10 nA. Known standards were used to quantify counts of each elements (Cl-turtupite; Ca, P-Durango apatite; F-halide; Na-amelia albite; MnO-bustamite; Y-xenotime; La, Ce-monazite; Sr-strontium titanite) using ZAF routine.

Elemental maps of apatite from samples X52, X38 and X59 were produced to determine elemental distribution. Mapping was conducted with the same EPMA system described above. Distributions of selected elements (Ce, Cl, Eu, F, Gd, La, Na, P, Si, Sm, Y) were acquired using the above described settings.

Trace element abundances of apatite of 11 samples were measured using the 213 nm laser ablation system coupled to a Thermo iCAP Q quadrupole mass spectrometer at Dalhousie University, Halifax Nova Scotia (Table 1). Prior to analyses, apatite were characterized using BSE imaging and targets were selected to avoid mineral inclusions and fractures. Analyses were conducted using raster line analyses of 35 µm in length with a beam size of 25 µm and a repetition rate of 10 Hz. Apatite were analysed using small lines in order to prevent fracturing of grains during ablation. Small (<30 µm) apatite were analyzed with traditional spot analyses with a beam size of 10 to 15 µm. Trace-element abundances were determined using an output energy of 170 mJ at 50% attenuation. Following data collection, signal-time intensity graphs were inspected for possible contamination by inclusions. Every 15 apatite analyses were bracketed by analyses of NIST (National Institute of Standard and Technology, synthetic glass) glass standards (NIST 610 and NIST 612) in order to correct instrumental drift and calibrate analyte sensitivities. Apatite standards (Ap-Sc, Ap and ApDG) and basalt standards (BHVO-1 and BIR) were

analyzed at the beginning and end of each run in order to correct drift. NIST610 was later used to calibrate analyte sensitives. Data reduction was conducted using the SILLS program, NIST610 was used as calibration standard and ratio of each isotope to counts of ^{40}Ca. NIST612, BHVO-1, BIR and apatite standards were used to ensure precision and accuracy of analyzed values.

Results

Apatite petrography

Skarn-hosted apatite of the Mactung deposit differ with respect to crystal form and habit, mineral associations, and paragenesis. Three distinct apatite types are classified (type-i, type-ii and type-iii) based on petrographic characteristics described below, as well as trace element chemistry described in subsequent sections. Most samples only contain one apatite type; however, sample X59 and X52 host both type-i and type-ii apatite. Additionally, detrital apatite in the form of relict calcium-phosphate nodules occur within samples and are characterized to compare with the later apatite.

Phosphate nodules

Detrital phosphate nodules occur in skarns from the Mactung deposit. Nodule are relict detrital apatite grains which are precipitated as concretions during diagenesis, these nodules form a major components of the 3D unit and are a minor components of the 2B, 3E and 3F units (Figure 1). Phosphate nodules occur as massive cryptocrystalline aggregates with either corroded edges or in sharp contact with surrounding phases (Figure 2). These are commonly hosted in garnet, quartz and pyrrhotite or surrounded by late mineral phases such as pyroxene, wollastonite and calcite (Figure 2). Calcite occurs as anhedral masses locally overprinting nodules. When associated with late quartz or pyrrhotite, portions of phosphate nodules appear to have been recrystallized forming

individual apatite crystal (Figure 2). The phosphate nodules show weak green luminescence (Figure 2).
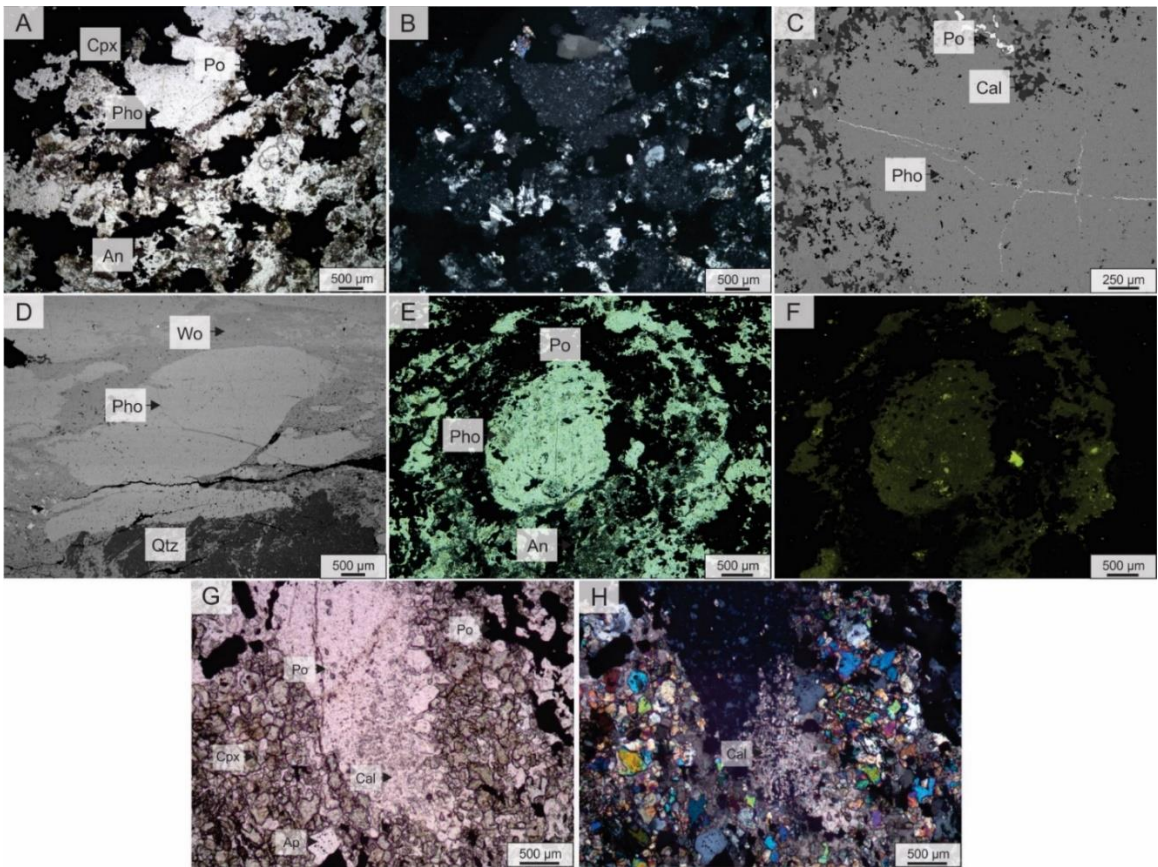
Figure 2: Photomicrographs showing early phosphate nodules overprinted by skarn. A) Photomicrograph of pyrrhotite and early phosphate nodules occurring with disseminated pyroxene and anorthite. B) XPL Photomicrograph showing cryptocrystalline appearance of phosphate nodules, this is only observable in XPL. C) A BSE images of a phosphate nodule thinning outward to small cryptocrystalline aggregates. D) A BSE image of a phosphate nodule in sharp contact with surrounding wollastonite. E) A photomicrograph of pyrrhotite and early phosphate nodule locally overprinted by anorthite and F) HCL of the same nodule showing dark green florescence G)Photomicrograph of a relict phosphate nodules surrounded by anhedral pyroxene H) When Imaged under XPL the same nodule appears to have been locally overprinted by disseminated calcite

Type-i apatite

Type-i apatite (samples X9, X27, X36, X38, X49, X53 and X59) are texturally and spatially associated with phosphate nodules in the units 2B, 3D and 3F (samples X9, X27, X36, X38, X49, X53 and X59). Phosphate nodules are not directly observed in the thin section for sample X59; however the association is inferred as the sample originates from the 3D unit that consist of phosphatic limestone containing abundant phosphate nodules. Type-i apatite occur in prograde skarns including garnet-pyroxene, pyroxene-pyrrhotite and pyroxene skarn in the upper ore zone (3D, 3F) and pyrrhotite skarn in the lower ore zone (2B) (Figure 1).

Type-i apatite overprint detrital phosphate nodules, but are paragenetically early with respect to all other phases. It occurs as inclusions in quartz, garnet or pyrrhotite, and is spatially associated with pyroxene, calcite, garnet and vesuvianite (Figure 3). When present, scheelite occurs in low abundance (< 1 modal %). Type-i apatite have euhedral to anhedral prismatic habit with variable grain-size (30 - 600 µm). The largest apatite grains (450 - 600 µm) are inclusions in massive pyrrhotite. Occasionally, apatite shows cusp and carry texture with pyroxene, indicating apatite replacement by clinopyroxene (Figure 3). Garnet-pyroxene skarn hosted apatite have subhedral habits, while pyroxene ± pyrrhotite skarn hosted apatite are euhedral and prismatic (Figure 3). Type-i apatite occasionally contain inclusions of quartz or calcite. Notable, native bismuth occurs interstitial to apatite in sample X36 (Figure 3).

Imaging of type-i apatite using hot cathodoluminescence reveal simple or oscillatory zoning. Cores of oscillatory zoned apatite are either non-florescent or show

weak blue or green florescence. The rims alternate between light and dark green oscillatory

zones, which brighten towards rims (Figure 3).
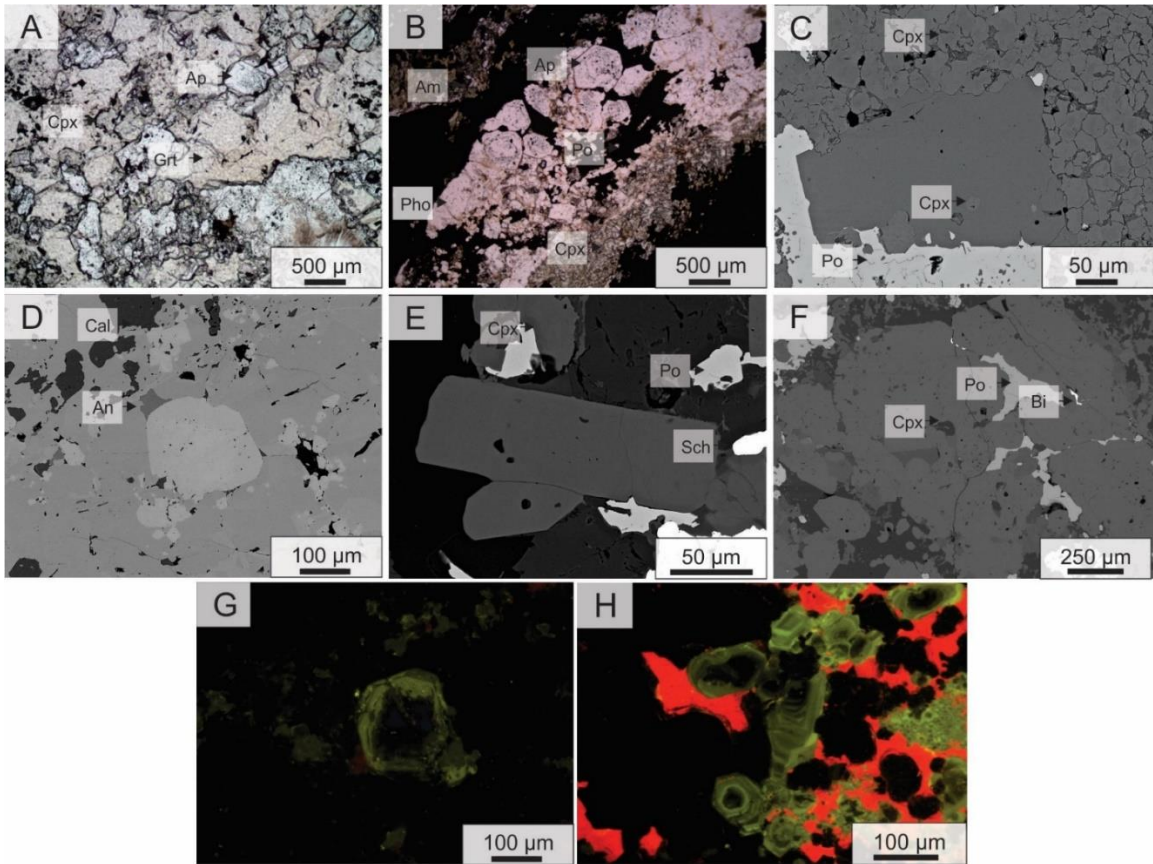
Figure 3: Plane polarized light (PPL) and Cl Photomicrographs as well as BSE images of type i-apatite. A) Subhedral apatite (Ap) and clinopyroxene (Cpx) as inclusions in garnet (Grt). B) Large euhedral apatite (Ap) and adjacent phosphate nodules (Pho) occurring with clinopyroxene and amphibole as inclusions in late pyrrhotite (Po). Amphibole occurs as an alteration product of early clinopyroxene. C) Large euhedral apatite exhibiting cusp and carry replacement by late clinopyroxene. D) Subhedral apatite inclusions in garnet. E) Euhedral apatite hosted in pyroxene skarn. Late anorthite (An) and quartz (Qtz) surround the grain. F) Large euhedral apatite with late bismuth (Bi). G) Simply zoned apatite showing weakly fluorescent blue core and green luminescent rims H) Oscillatory zone apatite with non-fluorescent cores and green florescent zoning brightening towards rims

Type-ii apatite

Type-ii apatite occur as disseminations in skarn, but are not associated with phosphate nodules. Sample X52 contains phosphate nodules; however, apatite is classified as type-ii because of its trace element chemistry (Figure 9). Type-ii apatite occur in the 2B (sample X52 and X63), 3C (sample X25 and X28) and 3D (sample X59) units hosted in prograde pyroxene or retrograde biotite and pyrrhotite skarns (Figure 1). This apatite is further subdivided into early and late type-ii apatite, based on their occurrence in prograde and retrograde skarn, respectively. Trace element analyses reveal that both early and late type-ii apatite occur in sample X28, this is consistent with the fact that the sample consist of prograde pyroxene skarn regionally altered to retrograde biotite skarn.

Early type-ii apatite (samples X25, X28, X59, and X63) occur as prismatic crystals in prograde pyroxene skarn. Pyroxene grains are abundant (20 - 35 modal %) with variable sizes (50 - 500 µm), other associated phases include titanite (<1 modal %) and calcite (<3 modal %). Pyrrhotite locally overprints the prograde skarn, it occurs in low abundances (<10 modal %) and is associated with adjacent to coeval plagioclase (Figure 4). Paragenetically late massive quartz overprints early pyroxene skarn in samples X59 and X63. This massive quartz flooding is associated with high grade scheelite mineralization in these select samples (3 modal %), individual scheelite grains are large (450 µm - 3.3 mm) and euhedral (Figure 4). Apatite have variable forms with sizes ranging from 75 µm – 1.6 mm and subhedral to euhedral prismatic habits. Early type-ii Apatite occasionally contain inclusions monazite (Figure 4). Hot cathodoluminescent imaging of type-ii apatite shows unzoned crystals with green to no fluorescence (Figure 4). It is notable that apatite included in pyrrhotite could not be imaged as the opaque mineral obscured the fluorescence. Orange

luminescent rim overgrowths occur on type-i apatite from sample X59, the quantification of the trace element composition of these overgrowths is similar to that of early type-ii apatite and warrants their classification (Figure 4).

Late type-ii apatite (samples X28 and X52) occur as prismatic inclusions in retrograde skarns. Apatite are associated with abundant pyrrhotite (15 - 30 modal %), fine grained plagioclase (5 – 10 modal %), clinozoisite, massive quartz (5 - 15 modal %) and trace pyroxene. Amphibole (< 7 modal %) and biotite (< 5 modal %) only occur in sample X28, biotite laths appear to have formed from the replacement of amphibole (Figure 4). Individual scheelite grains have a subhedral-anhedral form with a corroded appearance, grains occasionally appear to have been dissolved. Late type-ii apatite are small prismatic euhedral grains which occur as clustered inclusions in pyrrhotite or quartz (Figure 4). Apatite contain inclusions of pyrrhotite, uraninite and magnetite (Figure 4). Hot cathodoluminescence imaging of late type-ii apatite could not be conducted as opaque minerals obscured their fluorescence (Figure 4).
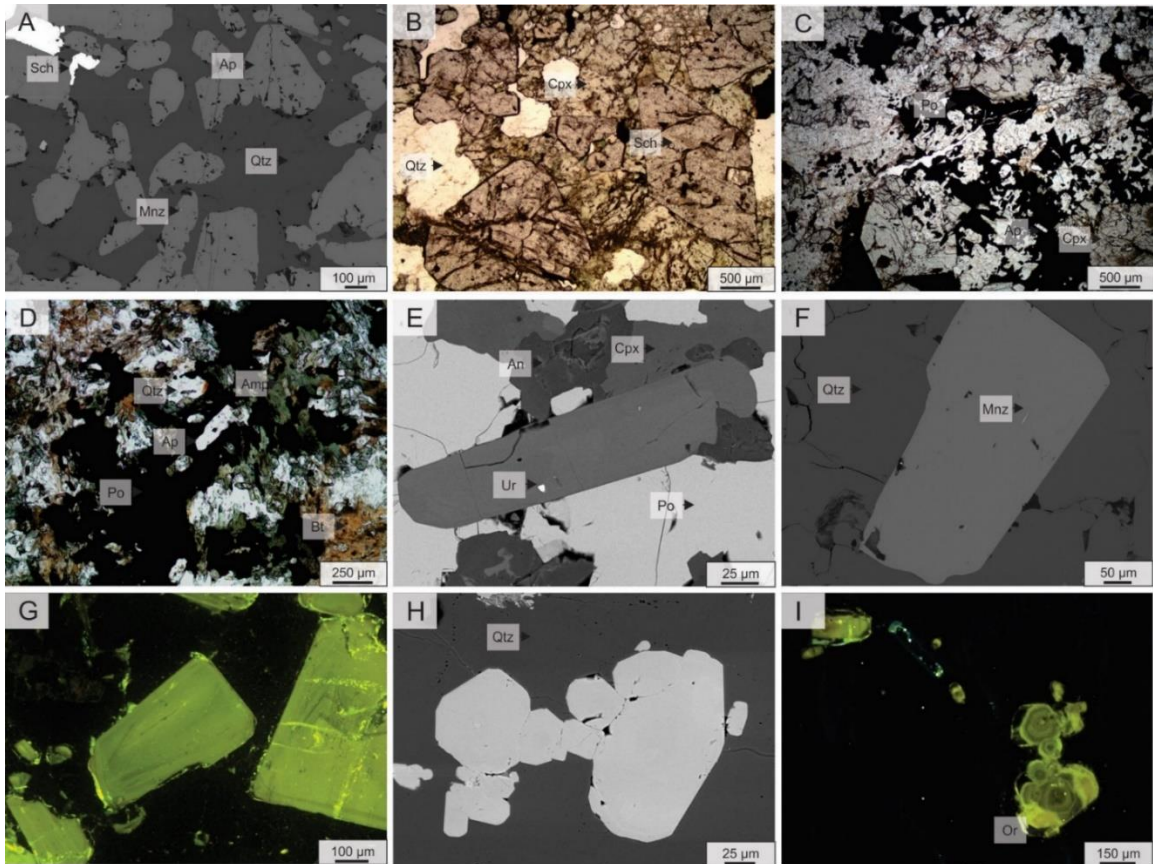
Figure 4: Photomicrographs (CL and PPL) and BSE images showing the petrography and occurrence of early and late type ii-apatite. A) Early type-ii apatite (Ap) are subhedral grains locally concentrated in massive flood quartz (Qtz), apatite contain monazite (Mnz) inclusions and are associated scheelite. B) Large euhedral scheelite occurring with massive clinopyroxene (Cpx) and quartz forming one of the highest grade assemblages observed. C) Common mineral assemblage associated with early type-ii apatite, small disseminated anorthite (An), large pyroxene and apatite are inclusion in paragenetically late massive pyrrhotite. D) Late amphibole extensively replaced by biotite occurring with quartz pyrrhotite and late type-ii apatite. E) Prismatic late type-ii apatite occurring with pyrrhotite, clinopyroxene and anorthite. Apatite contains an inclusion of uraninite. F) Large quartz hosted early type-ii apatite containing monazite inclusions G) Luminescent apatite showing unzoned bright green luminescence. H) Early type-ii apatite from sample X59 with I) orange apatite overgrowths. Chemical evidence suggest orange overgrowths are similar to early type-ii apatite, while the green cores displays trace element chemistry similar to type-i apatite.

Type-iii apatite

Type-iii apatite are associated with late crosscutting quartz-scheelite veins, which overprint pyroxene-pyrrhotite skarn assemblages (Figure 5). Type-iii apatite occur in various samples, yet only apatite from sample X21 were analyzed in this study. Its distinct occurrence and trace element chemistry warrants its discrete classification. The quartz-scheelite vein is composed of large euhedral scheelite, massive flood quartz and small disseminated apatite (Figure 5). Large euhedral scheelite grains concentrated along vein margins, scheelite is included in massive flood quartz (Figure 5). Apatite occur with scheelite along vein margins, grains are quite small with euhedral, prismatic habits and are free of inclusions. Type-iii apatite show green luminescence with simple to no zoning.

The vein assemblage crosscuts early phosphate nodules. The vein margins appear to have altered the prograde pyroxene skarn forming a rim of fine-grained anhedral plagioclase and clinozoisite along its contact (Figure 5). The two phases occur along the entire vein-skarn contact, clinozoisite is a minor component occurring interstitially to abundant plagioclases.
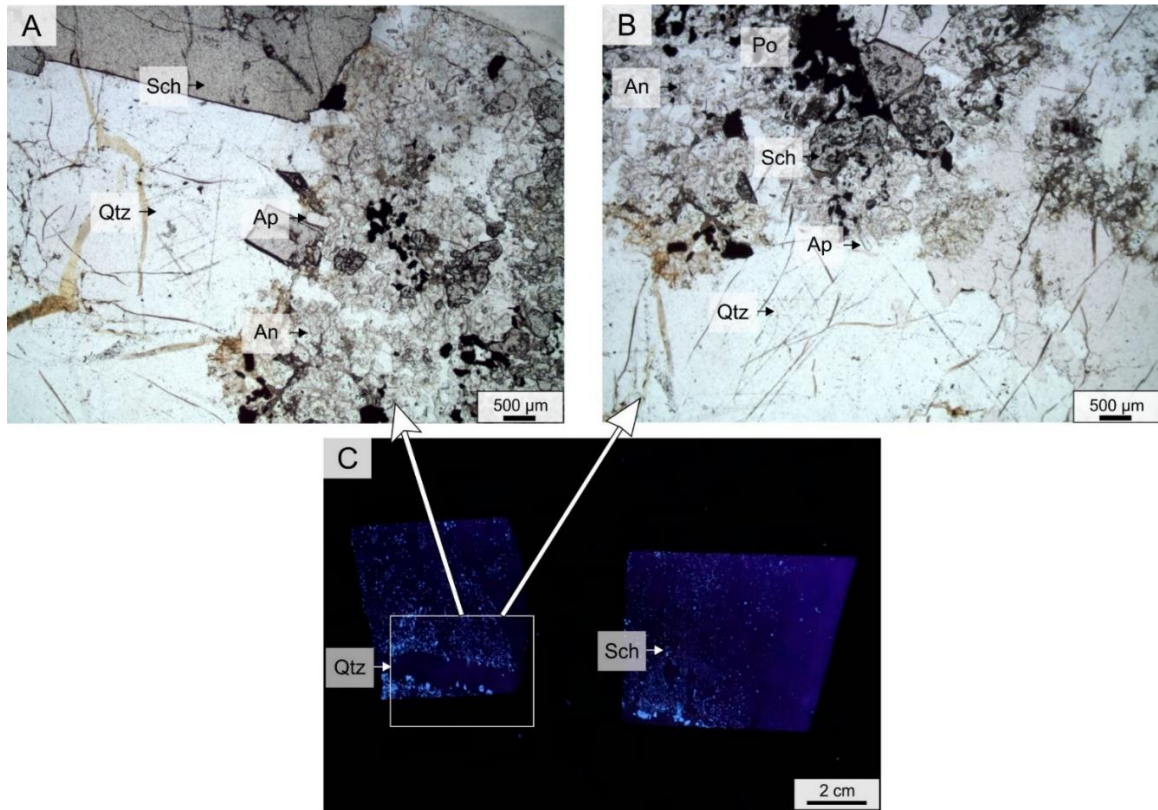
Figure 5: Photomicrographs (PPL) showing the petrography and occurrence of type-iii apatite. A) Prograde pyroxene-pyrrhotite is crosscut by a late quartz vein. Coarse grained scheelite and type-iii apatite are hosted in the quartz vein. B) Fine grained plagioclase and clinozoisite occur along the margin of the vein, these minerals are likely alteration products of the vein forming fluid. C) A fluorescent light photograph of drill core in which type-iii apatite occur. The blue fluorescent grains show high grade scheelite associated with the crosscutting quartz vein (non-fluorescent vein)

EPMA data

Apatite from six representative sample (X21, X9, X53, X52, X63, X59) were selected for EPMA analysis. A total of 128 data points were measured in order to quantify the major and minor element chemistry of the different apatite types and associated phosphate nodules. Mineral formula recalculations were conducted according to method proposed by Ketcham (2015) which assume that the monovalent anion site is behaving in an ideal fashion.

Type-i apatite

Major element chemistry of type-i apatite and phosphate nodules (samples X9, X53, X59, X21 and X52) is quantified through 69 EPMA measurements; Table 2 presents the averaged data as weight percent oxide per sample. Apatite contains almost stoichiometric CaO (average CaO = 55.34 ± 0.57 wt %) and P_2O_5 (average P_2O_5 = 42.27±0.65 wt %). Low concentrations of MnO (average MnO ≤ 0.20 wt %), Ce_2O_3 (average Ce_2O_3 ≤ 0.21 wt %) and Y_2O_3 (average Y_2O_3 ≤ 0.10 wt %) occur in type-i apatite. Concentrations of La_2O_3 (average La_2O_3 ≤ 0.08 wt %), NaO (average Na_2O ≤ 0.14 wt %, n = 11), SiO_2 (average SiO_2 ≤ 0.98 wt %, n = 7) and SrO (average SrO ≤ 0.01 wt %, n=1) are low or below the detection limit. Detectable NaO occurs in apatite from sample X59. Concentrations of SiO_2 are only above detection limits in apatite from sample X9, X59 and X53 as well as phosphate nodules from sample X52. Exceptionally high SiO_2 (max SiO_2 = 3.65 wt %) is detected in apatite rims in garnet-pyroxene skarn (sample X53). Type-i apatite contain low Cl (average Cl ≤ 0.1 wt %) with high F content (average F = 3.57 ± 0.52 wt %).

Acquired data was recalculated to atoms per formula unit (based on 25 oxygen) using the general chemical formula of the apatite super group formula $[Ca_{10}(PO_4)_6(OH,F,Cl)_2]$ (Table 2) in order to calculate OH content in apatite, as well as

determine the speciation and solid solution of apatite. Type-i apatite are primarily a solid solution of fluorapatite ($Ca_5(PO_4)_3F$) and hydroxylapatite ($Ca_5(PO_4)_3OH$) with the average structural formula: $Ca_{9.95\pm0.08}(P_{6.00\pm0.06}O_4)(F_{1.90\pm0.28}OH_{0.15\pm0.13})$. High F content indicates a predominantly fluorapatite component with low OH substitutions and essentially no Cl substitution. Apatite F content is often overestimate as F X-ray counts are affected by operating condition, analytical time and crystallographic orientation (Stock et al., 2015). Migration occurs in response to charge build up caused by the electron beam which leads F to migrate through interstitial crystallographic sites in the C-axis. Prior studies indicate that apatite crystals with their C-axis oriented parallel to the electron beam promote migration leading to overestimated X-ray counts of F. Analyzing grains with their C-axis oriented perpendicular to the electron beam limits this effect. The optimal analytical condition for calculating F are an acceleration voltage of 10 kV and a beam current of 4 nA (Stock et al., 2015). Unfortunately, these optimal analytical condition were not accounted for in this study; therefore, the F content is likely overestimated.

The evaluation of OH substitution is conducted through a stoichiometric estimate and is therefore dependent on the accuracy of calculated F. In 19 analyses from various samples (samples X9, X53, X21 and X52), calculation of OH based on atoms per formula unit gave negative values indicating an excess of F. Hence precise OH substitution cannot be evaluated for these select analyses. The highest OH component occurs in type-i apatite from sample X52 (average OH = 0.25 ± 0.14 apfu, average F = 1.84 ± 0.25 apfu) while apatite of sample X59 displays a high Cl component coupled with a high OH component (average OH = 0.23 ± 0.11 apfu and F = 1.76 ± 0.11 apfu). Apatite from samples X53 and X9, as well as phosphate nodules from sample X21, show the highest F component coupled

with the low OH and no Cl substitution (average F = 1.76 ± 0.11 apfu, average OH = 0.09 ± 0.10 apfu) (Table 2).

Type-ii apatite

Early and late type-ii apatite have similar major element chemistry, these two sub-types will therefore be grouped in this section. All type-ii apatite is quantified using 58 measurements of apatite in samples X52, X59 and X63 (Table 2). The concentration of CaO (average CaO = 55.08 ± 0.35 wt %) and P_2O_5 (average P_2O_5 = 42.92 ± 0.29 wt %) are near stoichiometric. Type-ii apatite contain low concentration of MnO (average MnO ≤ 0.26 wt %), Ce_2O_3 (average Ce_2O_3 ≤ 0.20 wt %), Y_2O_3 (average Y_2O_3 ≤ 0.36 wt %) and La_2O_3 (average La_2O_3 ≤ 0.08 wt %). Concentrations Na_2O (average Na_2O ≤ 0.63 wt %) and SiO_2 (average SiO_2 ≤ 0.24 wt %) are commonly below detection limits. Detectable Na_2O only occurs in apatite from sample X59 and detectable SiO_2 occurs in apatite from sample X63 and X59. Apatite SrO content is below detection limits for all analyses. Type-ii apatite contain high F (average F = 3.13 ± 0.32 wt %) and low Cl (average Cl = 0.02 ± 0.05 wt %).

Apatite mineral formula recalculations indicate that type-ii apatite are also a solid solutions fluorapatite and hydroxylapatite with the general structural formula: $[Ca_{(9.83±0.06)}(P_{(6.05±0.02)} O_4)(Cl_{(0.01±0.01)}F_{(1.64±0.17)}OH_{(0.35±0.17)})]$. High F content indicates a predominantly fluorapatite component with modest OH and negligible Cl substitution. Type-ii apatite hosted in sample X52 have a considerable OH component (average OH = 0.43 ± 0.13 apfu and average F = 1.57 ± 0.13 apfu), which was also observed in type-i apatite of the same sample. Moderate OH substitution occurs in apatite from sample X59 (average OH = 0.21 ± 0.14 apfu and average F = 1.78 ± 0.14 apfu) and X63 (average OH = 0.24 ± 0.12 apfu and average F = 1.72 ± 0.08 apfu). Only apatite from sample X59 contain

a detectable Cl component (average Cl ≤ 0.11 apfu). Atoms per formula unit recalculations are reported in Table 2.

Type-iii apatite

Major element chemistry of type-iii apatite is quantified through five measurements of apatite from sample X21 (Table 2). Type-iii apatite have the lowest CaO (average CaO = 54.57 ± 0.32 wt %) and P_2O_5 (average P_2O_5 = 41.98 ± 0.17 wt %) content, reflecting substitution of other elements. Apatite accommodate the highest concentrations of La_2O_3 (average La_2O_3 ≤ 0.15 wt %), Ce_2O_3 (average Ce_2O_3 ≤ 0.32 wt %) and Y_2O_3 (average Y_2O_3 ≤ 0.29 wt %) with modest MnO (average MnO=0.06±0.03 wt %). Concentration of (average SiO_2 ≤ 0.06 wt%, n = 3) are rarely detectable while SrO and Na_2O contents are always below detection limits

Type-iii apatite have a high F content (average F=3.25 ± 0.21 wt %) with essentially no Cl (average Cl ≤ 0.03 wt %). Type iii-apatite has an average formula $Ca_{(9.89±0.06)} Mn_{(0.01±0.01)} (P_{(6.01±0.02)} O_4 (F_{(1.74±0.11)} OH_{(0.26±0.12)})$. Hence, such apatite are a solid solution of fluorapatite and hydroxylapatite with a high fluorapatite component, a modest hydroxylapatite component and no chlorapatite component Table 2.

Table 2: Representative EPMA analyses of apatite for each sample. Phosphate nodules are averaged with type-i apatite. Atoms per formula unit (apfu) are calculated based on 25 oxygen.

sample	X52				X63		X59				X53		X9		X21			
	type-i		type-ii		type-ii		type-i		type-ii		type-i		type-i		type-i		type-iii	
Wt %	avg	1σ	avg	1σ	avg	1σ	avg	1σ	avg	1σ	avg	1σ	avg	1σ	avg	1σ	avg	1σ
Oxide	n=11		n=34		n=17		n=18		n=3		n=21		n=15		n=4		n=5	
CaO	54.90	0.38	54.97	0.35	55.33	0.23	55.34	0.27	54.97	0.08	55.47	0.65	55.44	0.72	55.45	0.16	54.57	0.32
Na_2O	0.00	0.00	0.00	0.00	0.00	0.00	0.02	0.03	0.25	0.27	0.00	0.00	0.00	0.00	0.00	0.00	0.00	0.00
SiO_2	0.01	0.02	0.00	0.00	0.01	0.06	0.09	0.26	0.08	0.03	0.17	0.78	0.00	0.02	0.00	0.00	0.03	0.02
Ce_2O_3	0.08	0.06	0.03	0.02	0.10	0.04	0.07	0.03	0.17	0.03	0.02	0.02	0.04	0.03	0.06	0.02	0.25	0.05
La_2O_3	0.02	0.02	0.01	0.02	0.03	0.03	0.02	0.02	0.05	0.01	0.01	0.01	0.00	0.01	0.00	0.00	0.11	0.04
MnO	0.09	0.08	0.18	0.04	0.03	0.02	0.03	0.02	0.06	0.03	0.02	0.02	0.01	0.01	0.01	0.01	0.06	0.03
Y_2O_3	0.03	0.02	0.01	0.01	0.03	0.04	0.04	0.03	0.31	0.06	0.01	0.01	0.02	0.02	0.07	0.02	0.23	0.08
P_2O_5	42.40	0.31	42.91	0.27	0.03	0.27	42.70	0.56	42.60	0.35	42.10	0.75	41.93	0.53	41.90	0.30	41.98	0.17
SrO	0.00	0.00	0.00	0.00	0.03	0.00	0.00	0.00	0.00	0.00	0.00	0.00	0.00	0.00	0.00	0.00	0.00	0.00
Cl	0.01	0.01	0.02	0.01	0.03	0.01	0.04	0.02	0.16	0.17	0.01	0.01	0.01	0.01	0.01	0.01	0.01	0.01
F	3.46	0.73	2.97	0.25	0.03	0.27	3.35	0.21	3.25	0.15	3.65	0.28	3.63	0.25	4.30	1.26	3.25	0.21
apfu Site M																		
Ca	9.89	0.04	9.82	0.05	9.83	0.07	9.88	0.06	9.83	0.04	9.98	0.08	10.02	0.04	10.02	0.03	9.89	0.06
Na	0.00	0.00	0.00	0.00	0.00	0.00	0.01	0.01	0.08	0.09	0.00	0.00	0.00	0.00	0.00	0.00	0.00	0.00
Ce	0.01	0.00	0.00	0.00	0.01	0.02	0.00	0.00	0.01	0.00	0.00	0.00	0.00	0.00	0.00	0.00	0.02	0.00
La	0.00	0.00	0.00	0.00	0.00	0.01	0.00	0.00	0.00	0.00	0.00	0.00	0.00	0.00	0.00	0.00	0.01	0.00
Mn	0.01	0.01	0.03	0.01	0.01	0.00	0.00	0.00	0.01	0.00	0.00	0.00	0.00	0.00	0.00	0.00	0.01	0.00
Y	0.00	0.00	0.00	0.00	0.01	0.00	0.00	0.00	0.03	0.01	0.00	0.00	0.00	0.00	0.01	0.00	0.02	0.01
Sr	0.00	0.00	0.00	0.00	0.00	0.00	0.00	0.00	0.00	0.00	0.00	0.00	0.00	0.00	0.00	0.00	0.00	0.00
Site T																		
P	6.03	0.02	6.06	0.02	6.05	0.02	6.03	0.05	6.02	0.03	5.98	0.08	5.99	0.01	5.98	0.01	6.01	0.02
Si	0.00	0.00	0.00	0.00	0.00	0.01	0.02	0.04	0.01	0.01	0.03	0.13	0.00	0.00	0.00	0.00	0.00	0.00
Site X																		
Cl	0.00	0.00	0.00	0.00	0.00	0.00	0.01	0.01	0.04	0.05	0.00	0.00	0.00	0.00	0.00	0.00	0.00	0.00
F	1.84	0.39	1.57	0.13	1.78	0.14	1.76	0.11	1.72	0.08	1.94	0.15	1.94	0.14	2.30	0.67	1.74	0.11
OH	0.25	0.14	0.43	0.13	0.21	0.14	0.23	0.11	0.24	0.12	0.10	0.09	0.09	0.11	0.07	0.12	0.26	0.12

LA-ICP-MS chemical data

A total of 128 measurements of 67 representative skarn hosted apatite grains were selected for trace element analysis by LA-ICP-MS. Although a large suite of trace elements in apatite were quantified, this study uses primarily REE to characterize the different apatite. Apatite contain high but variable concentrations of REE, with calculated ΣREE ranging from 140 to 12000 ppm with an average of 1600 ± 1600 (1σ) ppm; Y content ranges from 22 to 5600 ppm with an average of 490 ± 690 ppm. The three types of apatite have distinct REE compositions based on their ΣREE+Y abundance, chondrite normalized REE pattern, and relative ratios of La_N/Lu_N, La_N/Sm_N and Eu/Eu* (whereby Eu/Eu* = $\sqrt{Sm_N \ X \ Gd_N}$) .

Type-i apatite

Type-i apatite are characterized by variable total REE abundances with REE+Y values ranging from 320 to 4600 ppm with an average of 1300 ± 820 (1σ). Chondrite normalized (CN) REE patterns are similar for type-i apatite in different skarn assemblages and are characteristically negatively sloping with variable La_N/Lu_N ranging from 2.0 to 150 (average $La_N/Lu_N = 27 \pm 30$; 1σ), low MREE/HREE (average $La_N/Sm_N = 3.2 \pm 1.3$) and weak negative Eu anomalies (average $Eu_N/Eu*=0.6 \pm 0.2$), (Figure 6). Type-i apatite contain higher LREE (La to Gd) than HREE (Sm to Lu plus Y) with $\Sigma LREE_N/\Sigma HREE_N$ ratios ranging from 1.3 to 7.4 (average $\Sigma LREE_N/\Sigma HREE_N = 3.3 \pm 1.5$). Phosphate nodules from sample X52 show CN REE patterns similar to that of type-i apatite (Figure 6). Nodules have a high ΣREE+Y concentration (average ΣREE+Y = 167 ± 160) and a relatively moderate slope CN REE pattern ($La_N/Yb_N = 34 \pm 26$) (Figure 6). Representative analyses chondrite normalized REE from type-i apatite are shown in Table 3.

Trace element abundances in type-i apatite are reported in Table 4. Apatite contain variably high concentrations of Si (ranging 396 – 2360 ppm and averaging 1220 ± 409 ppm, 1σ), Fe (387 - 2170 ppm; 566 ± 240 ppm), Sr (21.5 – 1680 ppm; 212 ± 308 ppm), Th (3.27-192 ppm; 39.3 ± 35.4 ppm) and U (0.459 – 419 ppm; 56.1 ± 67.5 ppm) along with variable concentrations of Mg (2.99 – 368 ppm; 18.9 ± 46.2 ppm), Mn (16.1 – 442 ppm; 179 ± 106 ppm), Al (1.74 – 232 ppm; 23.3 ± 43.3 ppm), As (2.26 - 53.7 ppm; 11.5 ± 8.94 ppm), W (0.13 - 47.6 ppm; 7.12 ± 8.71 ppm) and Pb (0.16-8.83 ppm; 1.66 ± 1.20 ppm) (Table 4).

Trace element biplots of type-i apatite show a strong positive correlation between REE+Y and U+Th. A negative correlation occurs between Mn and As, and Mn and Sr as well as a broad negative correlation between Mn and W (Figure 7).
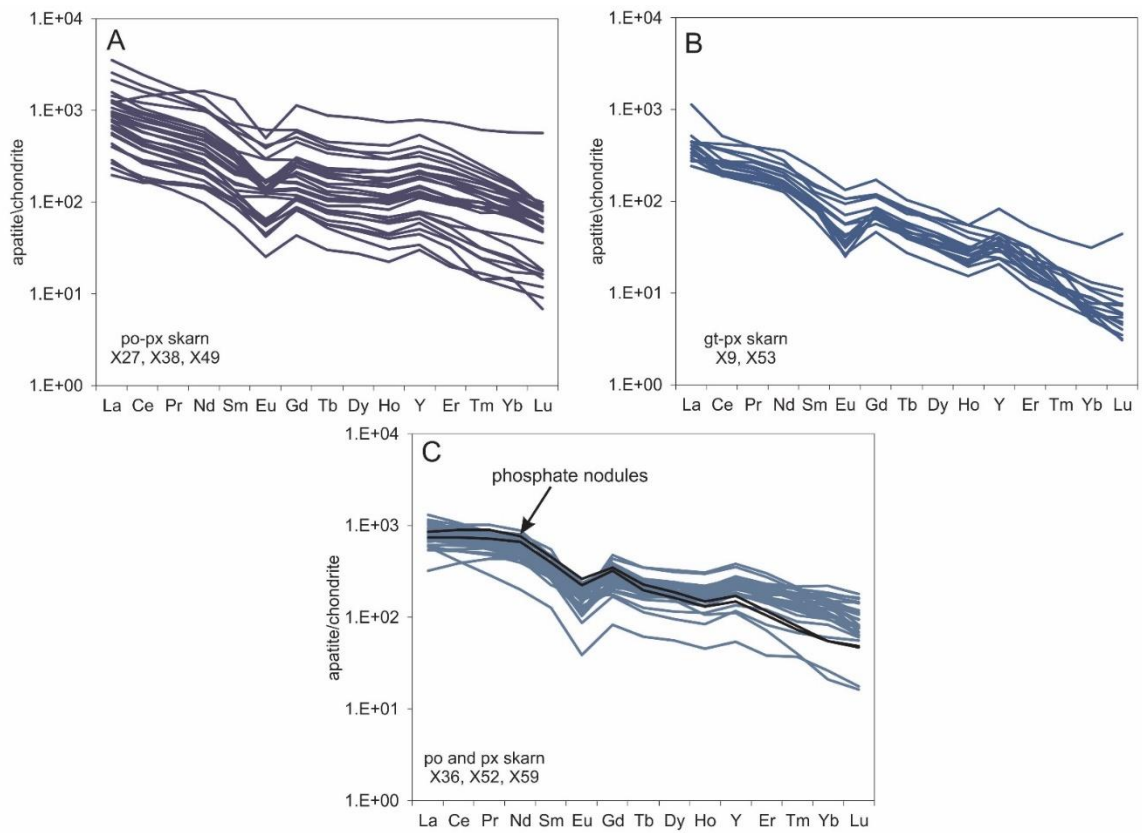
Figure 6: Chondrite normalized REE+Y diagrams for trace element spot analyses of type i-apatite from garnet-pyroxene skarn (gt - px), pyroxene-pyrrhotite skarn (px - po) and pyrrhotite skarn (py)

Figure 7: Trace element biplots of type-i apatite showing A) a strong negative correlation between Sr and Mn B) a strong negative correlation between As and Mn, C) a broad positive correlation between REE+Y and Mn, and D) a strong positive correlation between REE+Y and U+Th

Type ii-apatite

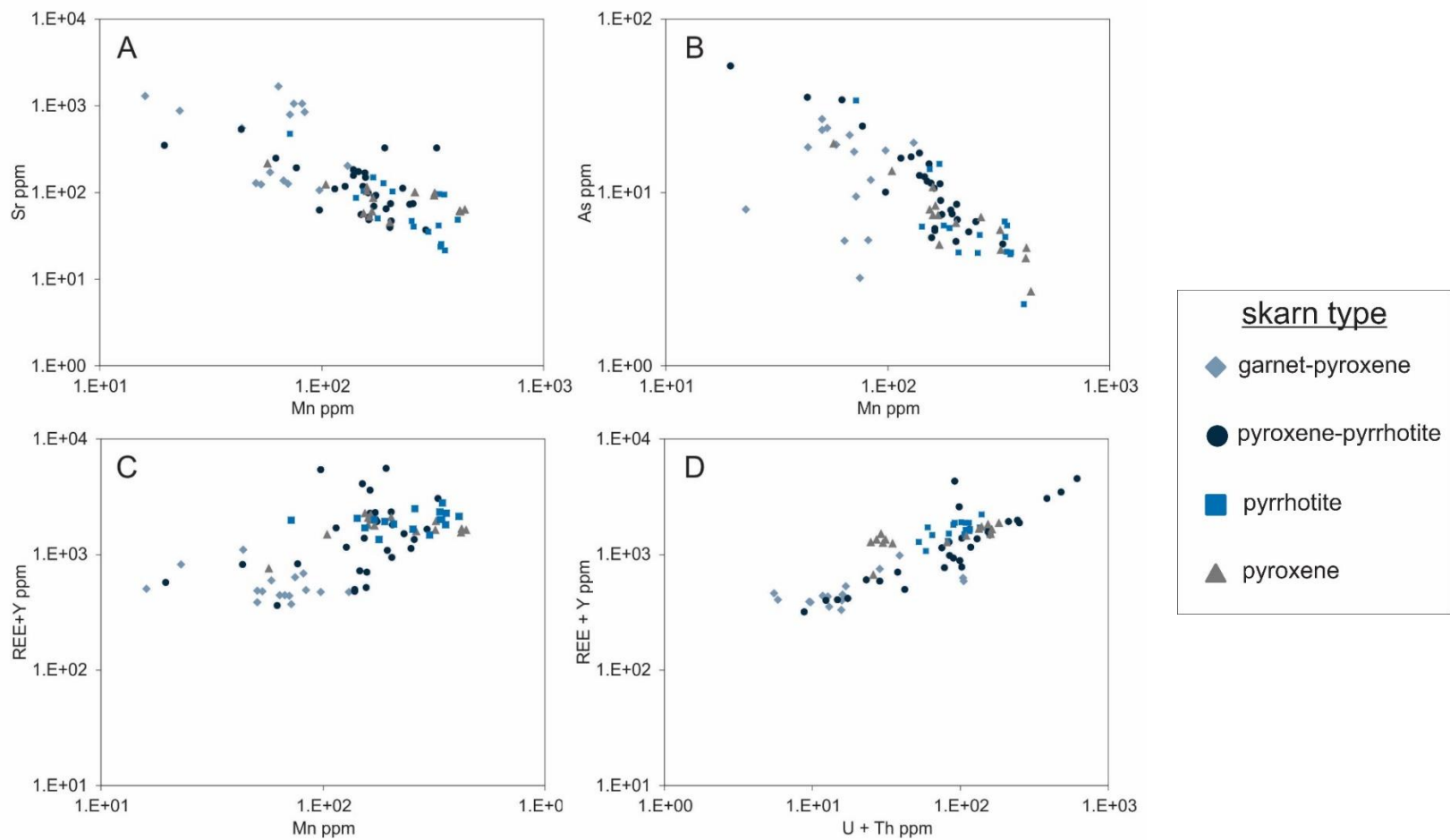A total of 28 analyses of prograde skarn hosted early type-ii apatite and 13 analyses of retrograde skarn hosted late type-ii apatite were measured (Table 3). Type-ii apatite are subdivided as they accommodate highly variable REE concentrations, and individual grains in a single sample may show contrasting compositions reflecting a continuum between two end-members: i) early type-ii apatite which show high flat lying CN REE patterns with positive Eu anomalies, and ii) late type-ii apatite which show MREE depleted CN REE patterns with positive Eu anomalies. Sample X28 apatite shows the continuum between the two endmembers; although, most samples contain apatite denote a single endmember (sample X25, X52, X59, X25 and X63). The REE+Y abundance and CN pattern correlate with mineral assemblage (i.e. prograde vs. retrograde skarn assemblage), supporting the subdivision of type-ii apatite into early and late subtypes.

Early type-ii apatite hosted in prograde pyroxene skarn samples X25, X28, X63 and X59 show flat lying CN REE patterns (average $La_N/Lu_N = 3.5 \pm 1.3$) with high variable $\Sigma REE+Y$ concentrations ranging from 1100 to 17000 ppm (average $\Sigma REE+Y = 4100 \pm 3500$) and strong negative Eu anomalies (average $Eu_N/Eu^* = 0.4 \pm. 0.2$) (Figure 8).

Late type-ii apatite hosted in retrograde skarn samples X52 and X28 show low $\Sigma REE+Y$ concentration (average $\Sigma REE+Y = 1100 \pm 850$ ppm) and positive or no Eu anomalies (average $Eu_N/Eu^* = 3.7 \pm 3.6$) (Figure 8). Late type-ii apatite show high La_N/Sm_N (average $La_N/Sm_N = 4.9 \pm 1.4$) and low Sm_N/Lu_N (average $Sm_N/Lu_N = 1.3 \pm 0.2$), reflecting low MREE content (Figure 8). Apatite from sample X52 are negative sloping with high LREE/HREE (average $La_N/Yb_N = 12 \pm 2.5$) whereas apatite from sample X28

are bowl shaped with low MREE/LREE (average $Sm_N/La_N = 0.1 \pm 0.1$) and MREE/HREE (average $Sm_N/Yb_N = 0.5 \pm 0.1$) (Figure 8).

Representative analyses of type ii-apatite trace elements are shown in table 4. early type-ii apatite have high variable Si (491 – 4290 ; 1560 ± 1120 ppm), Fe (457 – 11220; 672 ± 168 ppm), Mn (243 - 823; 552 ± 140 ppm), Mg (8.31 - 224; average = 59.7 ± 44.2 ppm), Th (up to 189; 29.7 ± 44.8ppm) and U (7.03 - 137; 39.3 ± 35.3 ppm) with moderately variable concentration of Sr (41.5 - 173; 71.1 ± 26.7 ppm) and low variable As (2.03 – 14.2; 5.62 ± 2.92 ppm), W (0.06-8.21; 0.85 ± 1.61 ppm), Pb (2.12 – 14.1; 6.26 ± 3.01 ppm).

Late type-ii apatite have comparatively lower Si (361 - 1870; 848 ± 584 ppm) and comparatively higher Mn (339 - 1410; 977 ± 363 ppm), Th (up to 888; 174 ± 288 ppm) and U (64.5 - 741; 233 ± 231 ppm) than early type-ii apatite. Apatite also have high variable Fe (645 – 1450; 1030 ± 275 ppm) and Mg (20.7 - 121; average = 75.9 ± 37.9 ppm) and Sr (69.9 - 134; 92.5 ± 16.23 ppm) and low variable As (2.03 – 12.4; 5.82 ± 4.71 ppm), W (up to 113; 17.3 ± 32.5 ppm), Pb (5.05 – 38.1; 19.3 ± 9.24 ppm).

Trace element biplots of type-ii apatite denote a strong positive correlations between Si and REE+Y, and Mn and Pb (Figure 9).
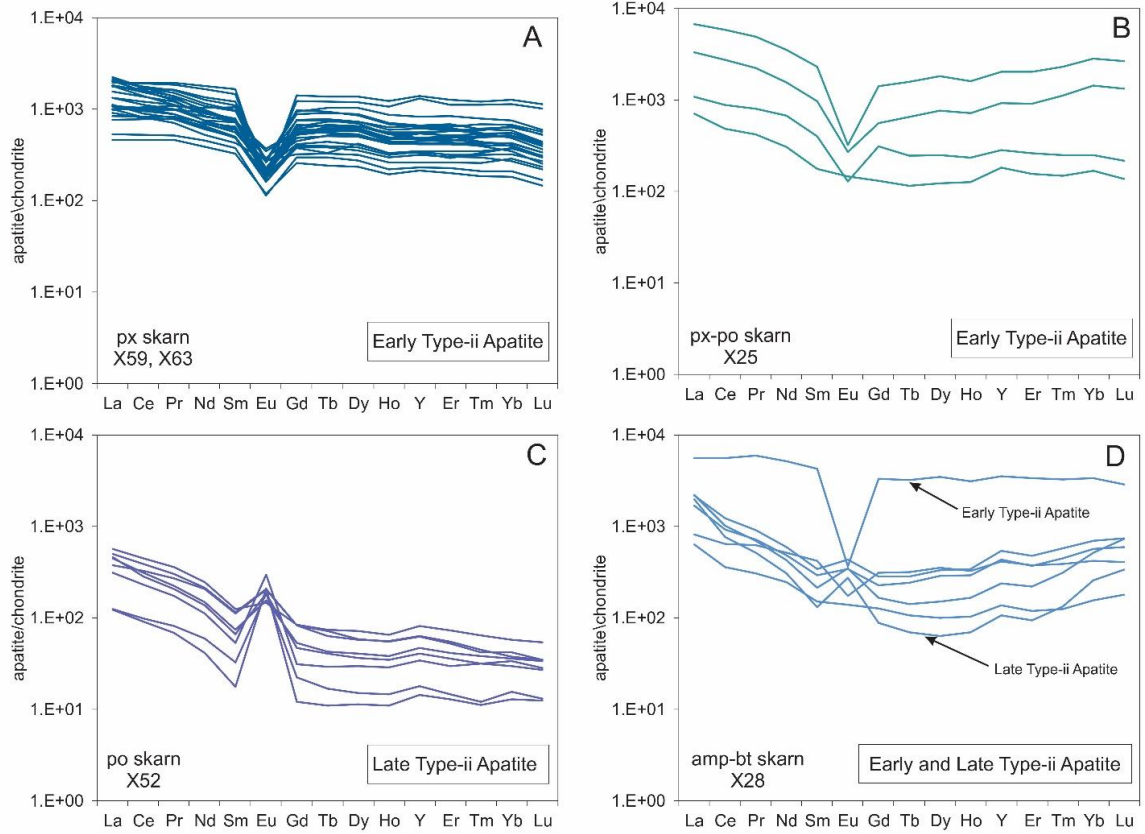
Figure 8: Chondrite Normalized REE and Y diagrams for trace element spot analyses of A) early type-ii apatite from pyroxene skarn (px), B) early type-ii apatite from pyroxene-pyrrhotite skarn (px - po) C) late type-ii apatite form pyrrhotite skarn (po) D) early and late apatite from altered amphibole biotite skarn (amp - bt)

Figure 9: Trace element biplots of type-ii apatite showing A) a strong positive correlation between Pb and Mn as well as B) a positive correlation between REE+Y and Si
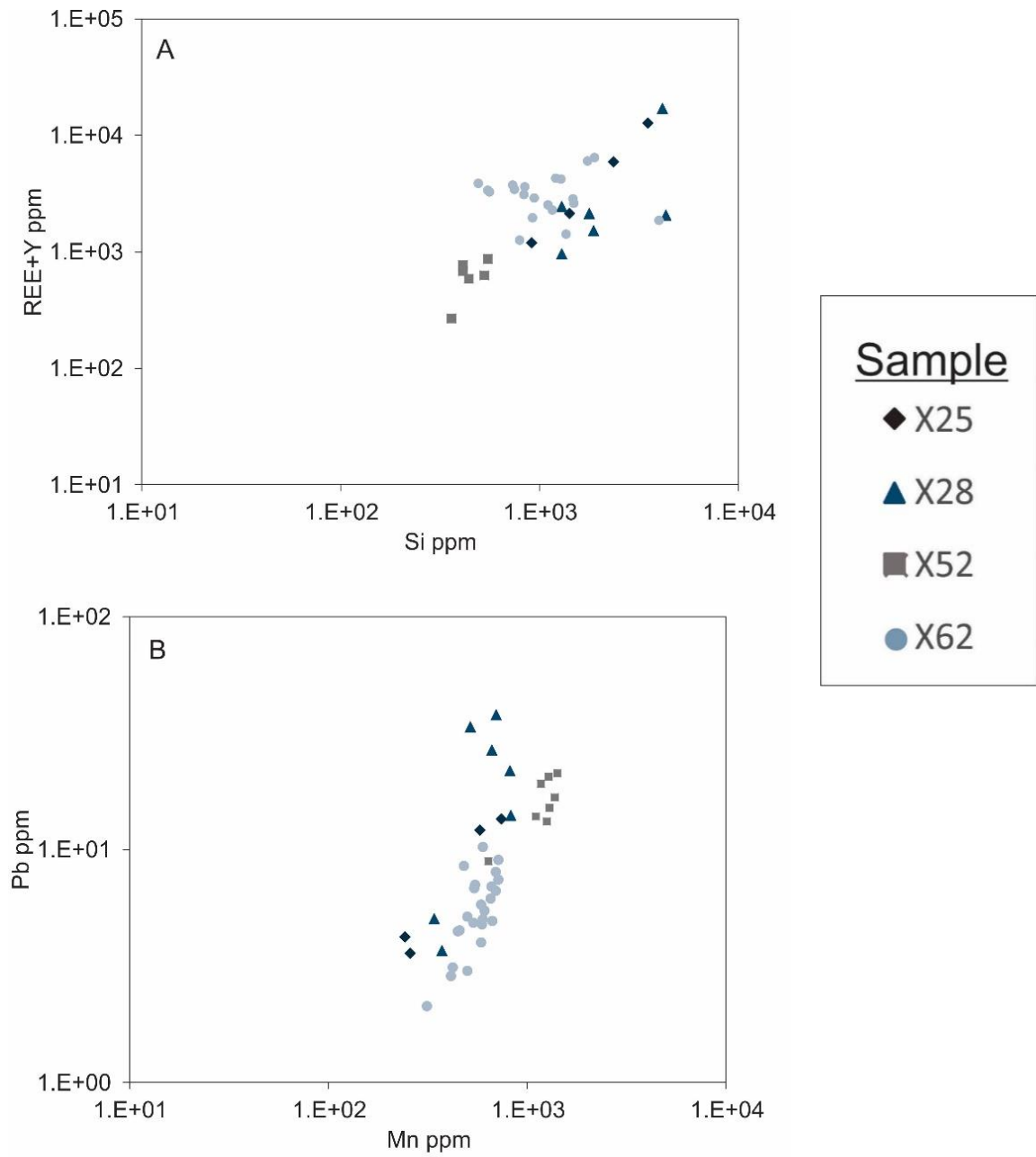
Type iii-apatite

Although type-iii apatite were abundant in quartz veins in samples XX and XX, only three measurements of type three apatite from sample X21 were collected due to the small grain size. This apatite has a distinct CN REE patterns with a very high $\Sigma REE+Y$ content (average $\Sigma REE+Y =7750 \pm 496$ ppm) and essentially no Eu anomalies (average $Eu_N/Eu^* =1.1 \pm 0.0$) (Figure 10). Chondrite normalized REE patterns of apatite are bell shaped with low MREE/LREE ($Sm_N/La_N=0.1\pm0.0$) and MREE/HREE ($Sm_N/Lu_N = 0.3 \pm 0.0$) (Figure 10).

Apatite contain high concentrations of Si (2180 – 2260 ppm), Mn (646 – 691 ppm), Fe (699 – 732 ppm), U (255 – 275 ppm) and Th (260 – 295 ppm) along with low Mg (31.1 – 33.1 ppm), As (6.00 - 6.13 ppm), Sr (91 – 99 ppm), Pb (19.2 – 19.4 ppm) and W(4.60 – 5.99 ppm). Representative analyses of trace element content are shown in Table 4
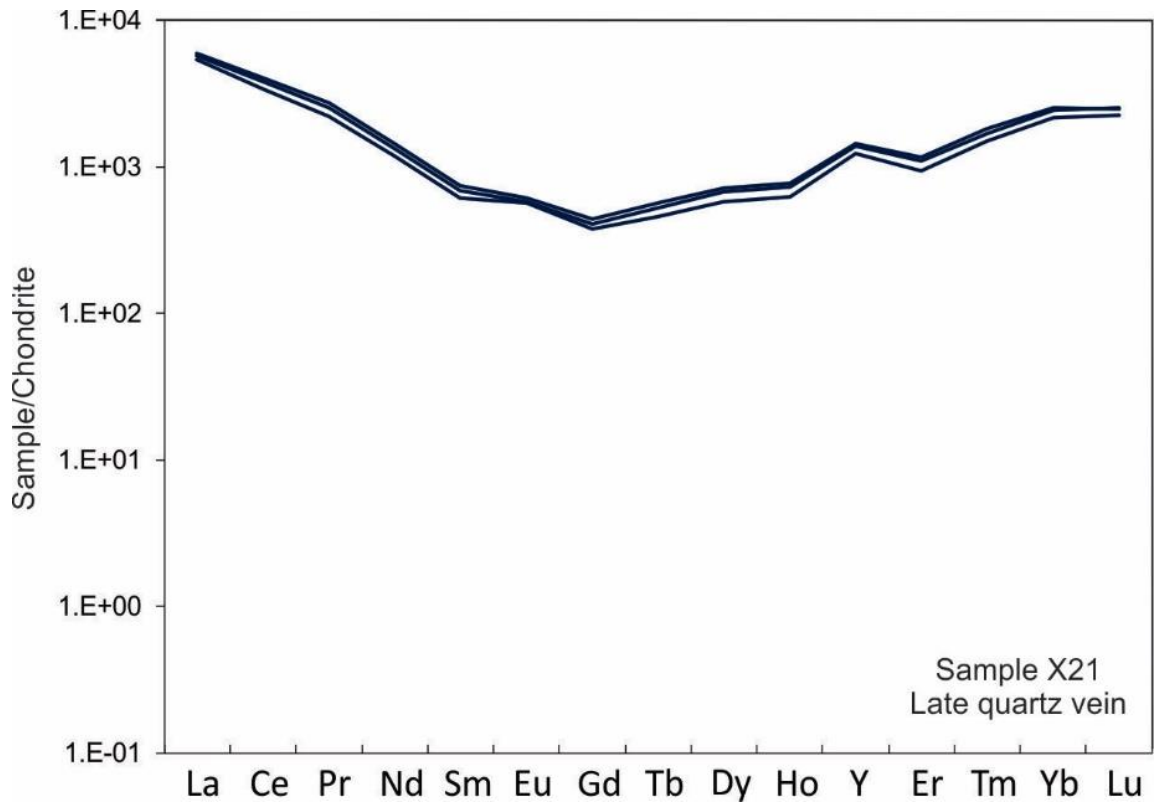
Figure 10: Chondrite normalized REE plus Y diagrams for trace element composition of type iii-apatite from a late crosscutting quartz vein

Table 3: Representative REE data of apatite from the Mactung deposit
Continued on next page

Sample	X49		X38		X36		X9		X53		X27	
Apatite Type	i		i		i		i		i		i	
Grain number	Min 2-2	Max 3-1	Min 1-3	Max 4-1	Min 4-2	Max 1-4	Min 1-3	Max 2-3	Min 2-2	Max 3-2	Min 8-1	Max 5-2
La	542	1200	290	872	853	686	375	1129	242	451	569	1281
Ce	368	1408	174	588	729	686	204	520	191	370	372	954
Pr	290	1559	136	459	614	636	161	393	157	319	284	791
Nd	220	1632	98	367	526	592	127	277	137	250	212	644
Sm	135	1314	54	205	258	445	62	126	81	152	116	376
Eu	125	499	26	169	87	144	27	94	43	106	115	161
Gd	118	1134	44	160	170	436	46	112	57	120	107	308
Tb	90	889	30	121	113	348	27	73	42	85	80	233
Dy	90	831	27	110	95	328	20	66	29	63	75	226
Ho	84	744	22	106	85	307	15	55	19	47	69	213
Y	111	792	30	130	117	385	21	83	24	38	79	251
Er	93	728	20	100	83	304	11	53	14	31	66	213
Tm	87	610	17	88	68	215	8	39	10	13	48	169
Yb	70	574	14	85	60	145	5	31	6	6	33	125
Lu	48	563	12	62	56	70	3	44	5	3	18	88
ΣREE+Y	460.4	4287.2	317.5	3479.0	1283.7	1885.4	353.9	975.5	979.6	885.8	586.4	1937.3
Eu*Eu	1.0	0.4	0.5	0.9	0.4	0.3	0.5	0.8	0.6	0.8	1.0	0.5
La/Sm	4.0	0.9	5.4	4.3	3.3	1.5	6.1	9.0	3.0	3.0	4.9	3.4
La/Lu	11.3	2.1	24.4	14.1	15.3	9.9	118.1	25.8	44.9	147.9	31.2	14.5
LREE/HREE	2.7	1.3	3.8	3.5	3.8	1.4	6.4	4.8	6.1	6.2	3.8	2.5

Table 3 continued

Sample	X25		X28		X63		X2				X59				X21	
Apatite Type	2		2		2		2		1		2		1		3	
	Min	Max	min	max	min	max	Min	Max	Min	Max	Min	Max	Min	Max	Min	Max
grain number	3-1	1-1	3-2	1-1	8-2	6-1	6-2	12-1	PO-2	1-2	1-2	9-1	4-1	7-1	1-3	1-2
La	710	6755	1984	5609	462	1780	124	568	855	1155	2013	1949	589	1003	1273	1405
Ce	487	5886	766	5585	464	1666	91	445	897	1010	1915	1944	408	799	2154	2544
Pr	421	4923	513	5924	462	1621	69	358	890	1018	1840	1928	288	725	202	249
Nd	305	3514	307	5194	386	1350	41	246	764	876	1646	1783	201	578	541	661
Sm	177	2308	131	4280	329	1207	18	124	455	462	1461	1656	127	327	95	115
Eu	145	321	276	365	119	274	210	147	261	204	179	165	39	180	33	36
Gd	131	1407	88	3312	258	972	12	84	350	355	1226	1417	83	265	74	87
Tb	115	1594	69	3211	242	939	11	74	227	212	1213	1380	61	205	17	21
Dy	123	1811	64	3502	235	855	11	71	189	153	1199	1378	56	194	142	174
Ho	126	1597	70	3101	193	683	11	66	149	106	1064	1225	46	189	34	42
Y	183	2031	107	3541	214	637	14	82	172	112	1318	1395	54	222	1929	2248
Er	155	2034	95	3392	199	625	13	73	117	72	1125	1269	38	192	150	185
Tm	148	2305	133	3272	185	554	11	64	80	40	1113	1215	37	159	37	45
Yb	169	2828	256	3349	181	482	13	58	55	21	1127	1273	26	138	358	419
Lu	138	2649	335	2890	146	364	13	54	47	16	1024	1144	18	107	56	62
ΣREE+Y	1106.1	12753.2	1456.0	17096.0	1215.7	4127.0	160.9	784.0	1723.0	1806.7	5982.4	6354.9	671.0	1664.7	7095	7867
Eu*Eu	1.0	0.2	2.6	0.1	0.4	0.3	14.3	1.4	0.7	0.5	0.1	0.1	0.4	0.6	1.2	1.1
La/Sm	4.0	2.9	15.2	1.3	1.4	1.5	7.0	4.6	1.9	2.5	1.4	1.2	4.6	3.1	8.8	8.3
La/Yb	5.1	2.5	5.9	1.9	3.2	4.9	9.9	10.5	18.1	71.0	2.0	1.7	33.5	9.4	2.4	2.3
LREE/HREE	2.1	1.5	3.6	1.2	1.6	1.7	5.8	3.6	3.2	4.7	1.1	1.1	4.1	2.3	36.9	36.9

Table 4: Representative trace element composition of skarn hosted apatite from the Mactung deposit

Sample	X25		X28		X63		X52				X59			
Apatite type	2		2		2		2		1		2		1	
Number of analyses	n=4		n=7		n=22		n=8		n=4		n=2		n=15	
	Min	Max	Min	Max	Min	Max	Min	Max	Min	Max	Min	Max	Min	Max
grain number	3-1	1-1	2-2	2-1	8-1	2-3	12-1	5-1	PO-1	1-2	1-1	9-1	4-1	4-2
Mg	8	27	14	38	10	102	41	100	7	7	-	28	-	32
Si	910	3505	4298	1296	1360	730	549	530	748	766	1400	1890	1010	1110
Mn	256	737	373	820	314	715	635	1277	154	171	104	549	57	442
Fe	503	645	657	703	548	776	715	1204	537	571	399	688	387	543
As	5	11	-	-	-	2	3	2	14	15	13	7	19	3
Sr	89	120	109	96	51	72	87	103	104	149	124	64	217	64
W	1	1	2	21	0	-	4	1	14	11	12	1	16	0
Pb	4	14	4	22	2	9	9	21	5	4	3	7	1	4
Th	30	189	28	311	2	17	9	12	16	14	38	64	14	10
U	49	128	39	336	8	47	65	140	48	46	43	54	12	21

Continued on next page

Table 4 continued

Sample	X36		X38		X49		X27		X9		X53		X21	
Apatite type	1		1		1		1		1		1		3	
Number of analyses	n=14		n=15		n=6		n=10		n=9		n=7		n=3	
analyses	Min x36-3-3	Max x36-2-3	Min x38-1-1	Max x38-6-2	Min X49-3-2	Max 3b-1	Min x27-2-1	Max x27-6-2	Min x9-1-1	Max x9-1-4	Min x53-1-3	Max x53-3-2	min x21-1-2	max x21-1-1
Mg	11	31	3	7	4	368	4	34	3	4	4	3	32	33
Si	1082	1517	2066	1202	1024	878	2363	1669	925	785	396	771	2179	2254
Mn	142	358	43	293	163	329	97	206	58	98	16	82	648	691
Fe	415	458	477	557	465	1240	556	971	496	495	419	523	699	732
As	6	5	35	-	6	5	10	7	19	17	-	5	6	6
Sr	88	21	538	37	52	329	62	47	172	107	1301	1065	94	99
W	1	1	6	1	1	2	5	4	19	15	0	8	5	5
Pb	5	4	3	6	7	4	25	8	3	2	0	1	19	19
Th	57	34	32	54	123	42	192	51	11	9	5	102	295	260
U	78	57	46	75	126	55	419	107	6	6	0	2	260	256

EPMA mapping

Elemental maps of five apatite grains were produced using the EPMA in order to discern the distribution of elements (e.g. zoning) in apatite: three type-ii apatite grains (grains X52-2, X52-4 and X52-6) with positive Eu anomalies, one type-i apatite grain with type-ii apatite rim overgrowths (grain X59-1) and one type-i apatite grain (grain X38-1) displaying oscillatory zoning in CL. Elemental zoning patterns are only observable in grains X38-1 and X59-1 (Figure 11) because the detection limits achieved using the EPMA were too low . Unfortunately, the grains are too small to analyze with the LA-ICP-MS, which has much lower detection limits. The map of sample X38-1 shows elevated Ce content in its core relative to rims (Figure 11). The maps from sample X59-1show elevated Y concentration in type-ii apatite overgrowths relative to type-i apatite cores; (Figure 11).
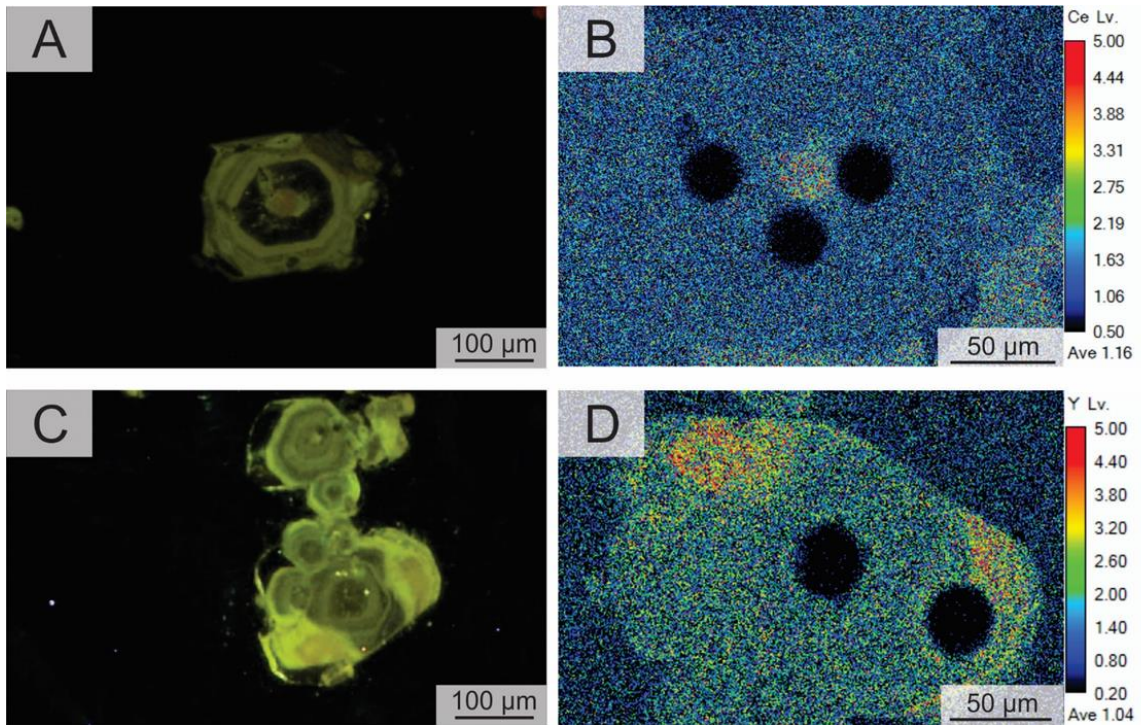
Figure 11: Elemental maps produced by EPMA of apatite. A) A CL image of type-i grain X38-1 showing detrital core and oscillatory zoned overgrowths. B) An elemental map of Ce showing with elevated Ce in the core. Black circles are pits from La-ICP-MS analysis. C) A CL image of type-i apatite grain X59-1 exhibiting orange type-ii overgrowths D) Rim overgrowths exhibit elevated Y detected in elemental maps. Note the scale bar for the elemental maps shows relative abundance and is not quantitative.

Discussion

Apatite from the Mactung deposit are classified into three chemically and paragenetically distinct generations, each of which record different stages in the evolution of the Mactung deposit. Considering paragenetic and mineral associations, as well as trace chemistry, the following interpretations are proposed: type-i apatite are non-hydrothermal and record contact metamorphism associated with the early intrusion of a pluton, while type-ii and type-iii apatite are hydrothermal and record the evolution of hydrothermal skarn fluids.

Origin of non-hydrothermal type-i apatite

Type-i apatite are hosted in prograde skarn assemblages and are spatially associated with phosphate nodules (Figure 2). This suggests that type-i apatite crystallized early in the history of the deposit, after diagenesis of the limestone but prior to skarn mineralization. Therefore, type-i apatite is interpreted to have formed during contact metamorphism of the host rock.

Type-i apatite exhibit similar REE patterns as the phosphate nodules, as shown for apatite and phosphate nodules in sample X52 (Figure 6). The spatial and chemical association suggests that type-i apatite are either recrystallization products of the phosphate nodules, and/or both generations of apatite equilibrated during the crystallization of type-ii apatite at some point after diagenesis of the host limestone.

Prior studies have shown that the chemistry of phosphate nodules can be altered by secondary processes such as metamorphism and metasomatism (e.g., McArthur and Walsh, 1985). In order to evaluate whether type-i apatite inherited its REE from the phosphate nodules, or if the apatite and phosphate nodules equilibrated with the environment during metamorphism, the apatite REE values (normalized to North American Shale Composite,

NASC; Gromet et al., 1984) are compared to the REE of phosphate nodules from Howards Pass in the Selwyn Basin (Gaad et al., 2016). Data from this study was selected as these nodules originate from strata of similar age and locality, and are unaffected by metamorphism or hydrothermal activity (Gaad et al., 2016). Phosphate nodules from Howards Pass have weakly negative sloping NASC REE patterns ($La_N/Lu_N = 2.0 \pm 0.7$) with negative Ce anomalies ($Ce/Ce^* = 0.6 \pm 0.1$) and no Eu anomaly ($Eu/Eu^* = 1.0 \pm 0.2$) (Figure 12). Type-i apatite have negative sloping NASC REE signatures ($La_N/Lu_N = 3.75 \pm 4.05$) with weak negative Ce anomalies ($Ce/Ce^* = 0.92 \pm 0.06$) and Eu anomalies ($Eu/Eu^* = 0.8 \pm 0.2$) (Figure 12). Type-i apatite show a much larger range of REE than phosphate nodules due to their variable HREE content (Figure 12). This can be attributed to variations in phosphate nodule chemistry as well as fraction by co-crystalizing apatite and Garnet. In comparison, the NASC REE patterns of type-i apatite are very similar with those from Howards Pass (Figure 12). This supports the interpretation that type-i apatite are non-hydrothermal in origin and derived from the recrystallization of detrital phosphate nodules during contact metamorphism associated with the intrusion of the nearby plutons. Variations in the REE chemistry of type-i apatite can be attributed to variations in phosphate nodule chemistry.
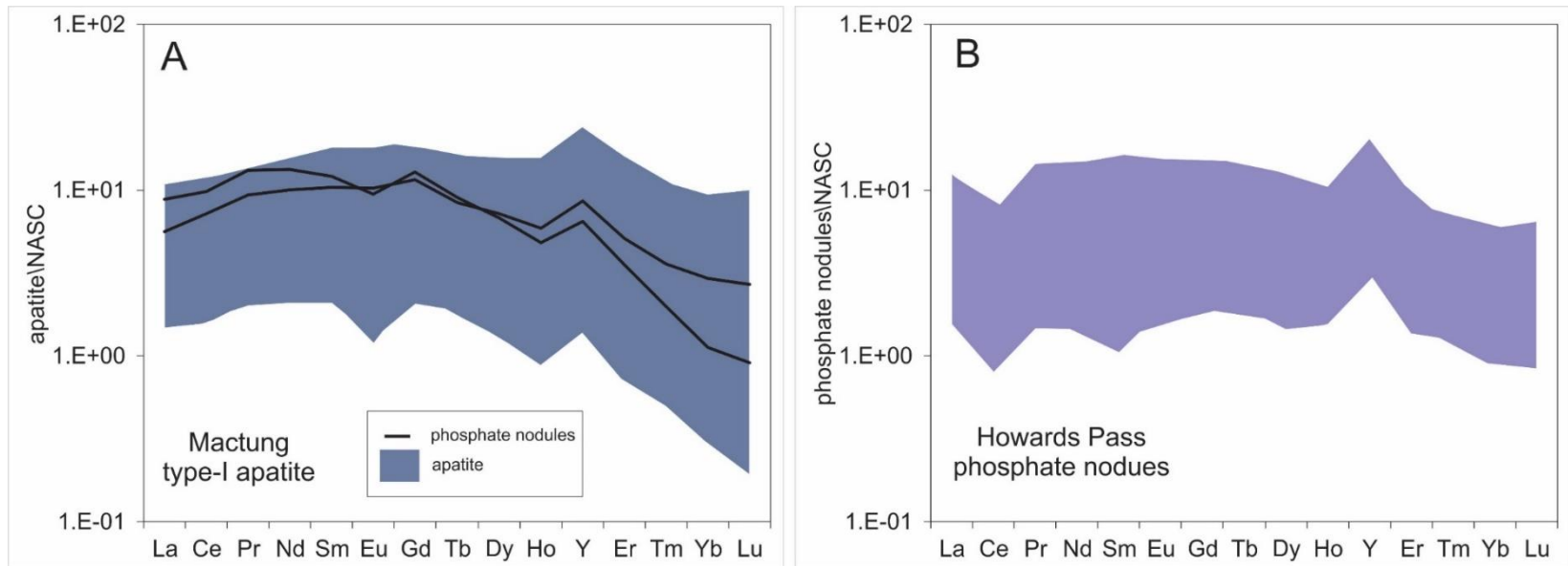
Figure 12: NASC normalized REE patterns of A) apatite and phosphate nodules from the Mactung deposit and B) phosphate nodules from Howards Pass (Gaad et al., 2016)

Origin of hydrothermal type-ii and iii apatite

Type-ii apatite are further subdivided based on mineral assemblages and trace element (REE) chemistry. Early type-ii apatite occur in prograde pyroxene ± pyrrhotite skarn and is characterized by relatively high total REE+Y, and flat lying CN REE with negative Eu anomalies. Late type-ii apatite occurs in retrograde amphibole-biotite skarn assemblages and exhibit MREE depleted CN REE signatures with positive Eu anomalies (Figure 13). While most samples exhibit only one generation of type-ii apatite, both CN REE signatures occur in individual apatite grains from sample X28 (Figure 13). This sample comprises prograde pyroxene-pyrrhotite skarn crosscut by a late, retrograde sulfide vein and the regions adjacent to the vein are altered to amphibole-biotite skarn.

Both early and late type-ii apatite are in textural equilibrium with associated skarn minerals indicating that apatite are hydrothermal in origin. Owing to the fact that early and late type-ii apatite have different chemical signatures and paragenetic associations, their CN REE signatures must reflect separate stages in the systems hydrothermal evolution. The occurrence of the two distinct REE compositions of in type-ii apatite can be attributed to a single fluid undergoing Rayleigh fractionation, or two chemically distinct ore fluids.
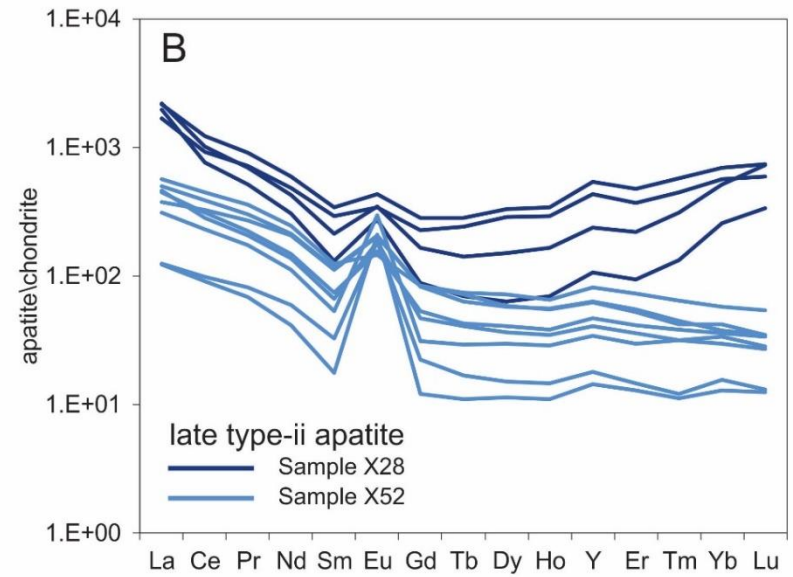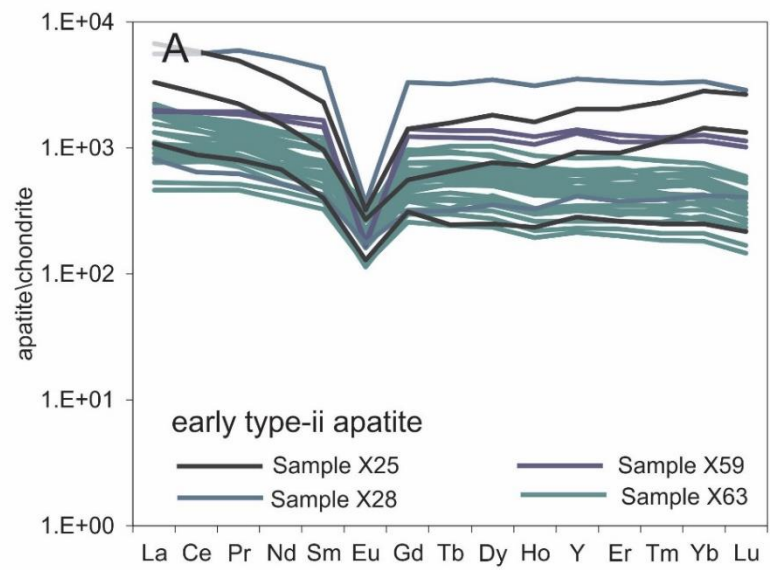
Figure 13: CN REE signatures of A) prograde skarn hosted early type-ii apatite and B) retrograde skarn hosted type-ii apatite

The fractionation of REE by earlier or coeval phases, or apatite itself, may explain the different REE composition of early and late type-ii apatite. Associated skarn phases that partition REE were analyzed via LA-ICP-MS to evaluate their influence (Appendix). Skarn hosted clinopyroxene, titanite and scheelite are coeval with, or closely preceded, apatite crystallization. If these coeval phases influenced the REE composition of type-ii apatite these would should MREE enriched CN REE patterns with positive Eu anomalies. Such patterns would indicate that fractionation of the ore fluids by skarn minerals cause the variable CN REE signature's recorded in type-ii apatite. However, all analyzed skarn minerals show lower total REE than all type-ii apatite. Scheelite CN REE are weakly sloping to flat lying with weak Eu anomalies while titanite show flat lying CN REE with weak Eu anomalies and clinopyroxene contain very low REE concentrations. Hence, the CN REE patterns of these phases indicate that these minerals did not affect the REE composition of apatite (Figure 14).

The CN REE signatures of both early and late type-ii apatite may reflect Rayleigh fractionation of a single fluid by apatite. Considering apatite has higher partitioning coefficients for MREE over LREE, HREE and Eu^{2+} (Ayers & Watson, 1993; Watson & Green 1981), fractionation of REE from a single fluid by apatite could generate an evolved fluid that is MREE depleted with positive Eu anomalies. Similar fractionation effects were invoked by Brugger et al. (2000) to explain CN REE patterns occurring in scheelite and apatite from the Mt. Charlotte and Drysdale Au deposit in Australia. Apatite and scheelite were oscillatory zoned, the cores of both minerals were MREE enriched with no Eu anomaly while rims were MREE depleted with positive Eu anomalies (Figure 15), similar as early and late type-ii apatite of this study. Brugger et al. (2000) conclude that the contrasting CN REE signatures of the early and late generations are produced by

fractionation of REE by scheelite/apatite. The proposed model suggest that the CN REE of early scheelite and apatite reflect that of the initial fluid, and that MREE were preferentially incorporated relative to Eu^{2+}. This produced late apatite and scheelite with positive Eu anomalies a low MREE (Figure 16). The CN REE of both early and late type-ii apatite do appear to reflect a continuum between two end member compositions similar to that recorded by Brugger et al., (2000). However, the change from a strong negative to strong positive Eu anomaly observed in type-ii apatite is inconsistent with fractionation by apatite as shown by Brugger et al. (2000). Prior experimental studies have also shown minimal contrast in the partitioning of Eu^{2+} and REE^{3+} between the fluid and apatite, as described in the *Apatite Mineral Chemistry* section of the *Background* (Ayers & Watson, 1993). Apatite inherit the Eu anomalies of their source fluid, fractionation can increase the contrast in partitioning between Eu and REE leading to a minimal increase in Eu anomalies (Ayers & Watson, 1993). Thereby, Rayleigh fractionation can produce weak negative Eu anomalies from strong negative anomalies or strong positive Eu anomalies from weak positive anomalies (Brugger el al., 2000; Ayers & Watson, 1993). However, it cannot solely account for the occurrence of both positive and negative Eu anomalies, and differences in relative MREE abundance, in type-ii apatite from the Mactung deposit. Alternatively, such CN REE patterns may be derived from two chemically distinct ore fluids, one with high total REE+Y, a negative Eu anomaly and flat lying CN REE pattern, and another low total REE+Y, MREE depleted fluid with no or a positive Eu anomaly. Preliminary scheelite REE data additionally suggest the occurrence of two chemically and paragenetically distinct generations and is consistent with scheelite derived from two different ore fluids
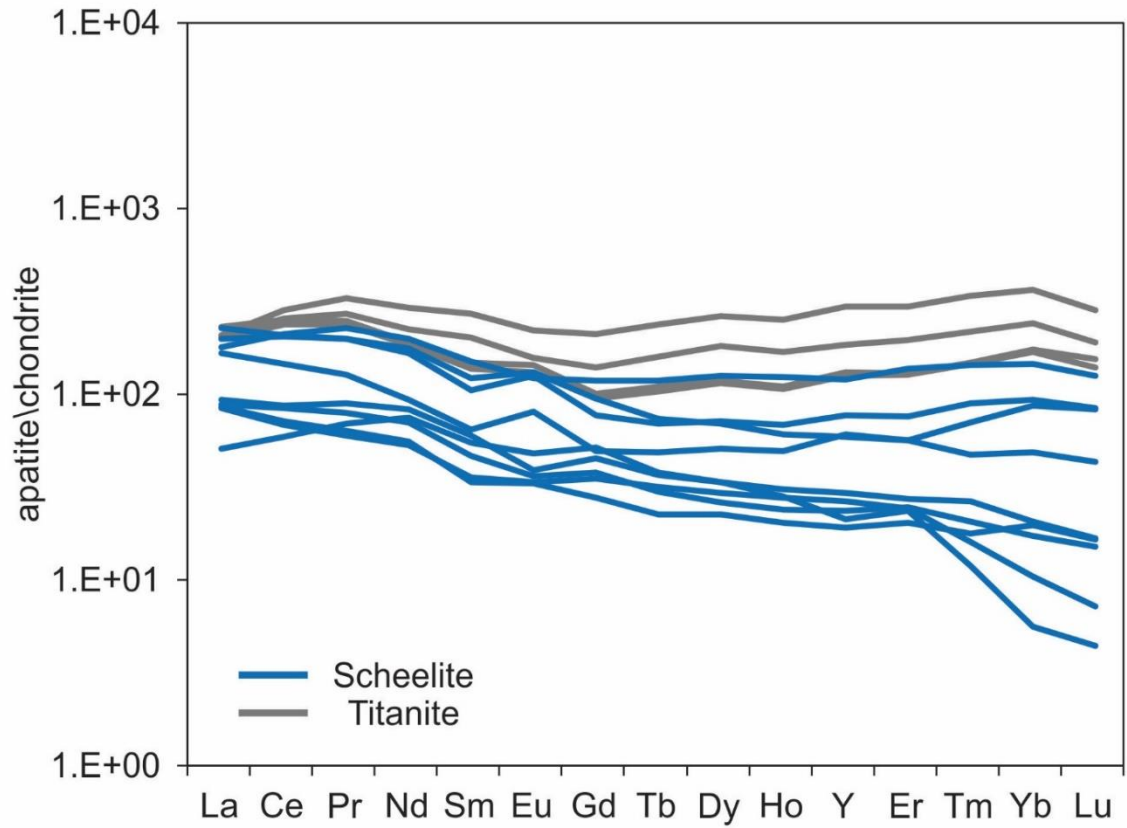
Figure 14: CN REE patterns of skarn hosted titanite and scheelite, REE diagrams indicate that neither phases affected the REE composition of type-ii apatite. Pyroxenes were also analyzed but are excluded from the figure due to their low REE content
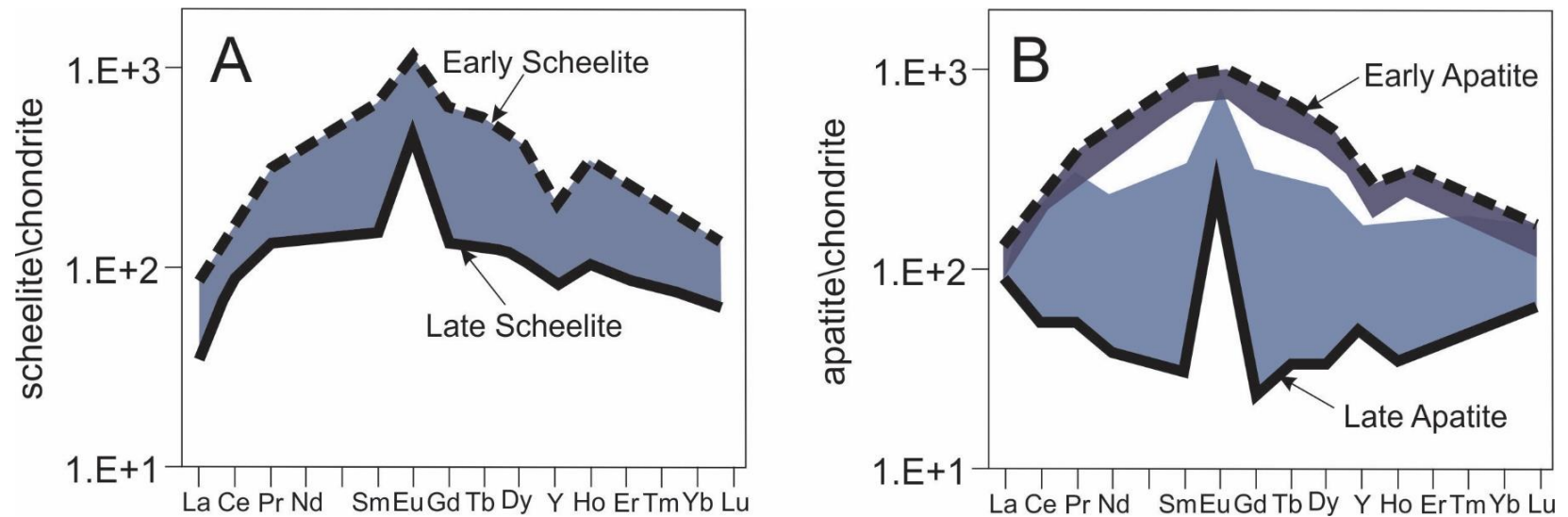
Figure 15: CN REE patterns of early and late scheelite and apatite from the Mt. Charlotte and Drysdale gold deposit located in the Kalgoorlie gold district of Western Australia, modified from Burger et al., (2000). A) Early scheelite show MREE enriched patterns with positive Eu anomalies while late scheelite show MREE depleted patterns with strong positive Eu anomalies. B) Early apatite shows MREE enriched pattern with no Eu anomalies, while late apatite show an MREE depleted patterns with positive Eu anomalies. The CN REE patterns of both scheelite and apatite appear to reflect a continuum between two end member compositions. Such variations in CN REE signatures can be explained by two chemically distinct fluids or Rayleigh fractionation.
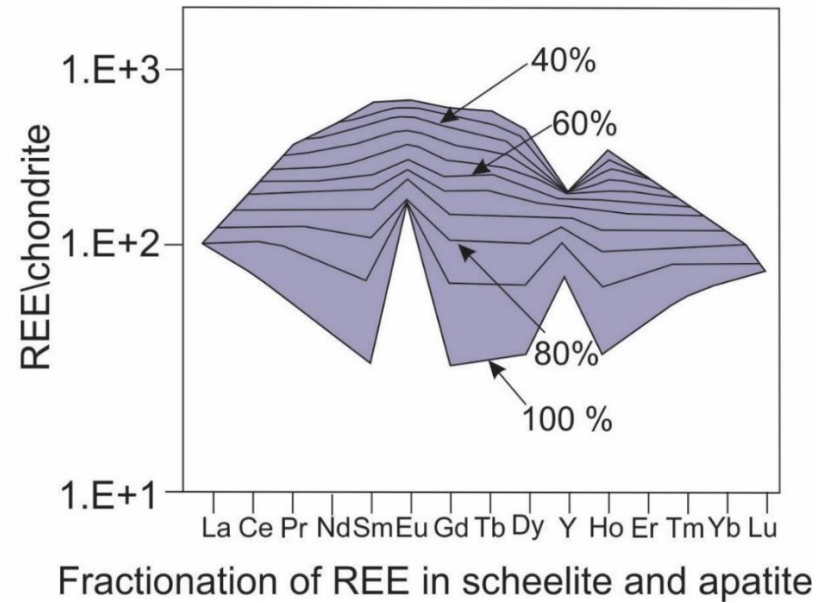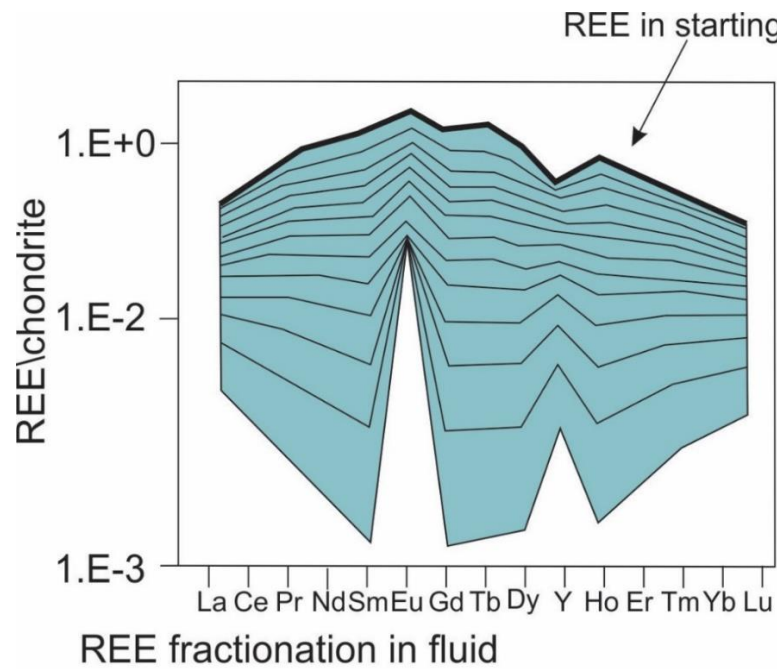
Figure 16: Rayleigh fractionation of REE from the fluid (A) by scheelite (B). The REE content of early scheelite reflects that of the of the unfractionated fluid. With increasing crystallization of apatite and scheelite, the REE content of the fluid and scheelite change accordingly. Modified from Bruger et al., 2000

Positive and negative Eu anomalies were recorded in skarn hosted apatite from Cantung and are attributed to multiple ore fluids (Adlakha et al., 2018). Positive Eu anomalies with MREE depletion in apatite were attributed to a fluid derived from an amphibole saturated mafic magma, while negative Eu anomalies were attributed to a fluid derived from a felsic melt which had fractionated plagioclase (Adlakha et al., 2018). The CN REE signatures of apatite from Cantung closely resemble those of early and late type-ii apatite from the Mactung, this may indicate ore fluids of similar origin. Yet, apatite from Cantung show oscillatory or simple zoning, such zoning is not observed in apatite from Mactung. Apatite zoning at Cantung corresponds to the alternation of the flat lying CN REE pattern with negative Eu anomalies (i.e. early type-ii apatite from this study) and MREE depleted CN REE patterns with positive Eu anomalies (i.e. late type-ii apatite from said study). The occurrence of similar REE patterns at Cantung may indicate that a similar genetic evolution for both deposits.

The quartz-scheelite vein hosted type-iii apatite show a distinct bowl shaped CN REE patterns with high ΣREE+Y, low MREE and no Eu anomaly. The CN REE of type-iii apatite could be related to the late type-ii apatite fluid, considering both exhibit MREE-depleted signatures (Figure 17). However, the timing of these two generations of apatite require evaluation as their relationship to each other and scheelite mineralization is unclear. Elemental distribution maps by micro-XRF of thin sections X21 (Figure 18) and X25 (Figure 19) elucidate the relationships between type-ii and type-iii apatite. These two samples were selected as they both contain prograde pyroxene-pyrrhotite skarn that is crosscut but a late quartz vein and host early type-ii and type-iii apatite previously analyzed in this study (Figure 18 and Figure 19). In sample X25, early type-ii apatite are hosted in the pyroxene-pyrrhotite skarn and in sample X21 type-iii apatite are hosted in the

crosscutting quartz vein (Figure 18 and Figure 19). The XRF images from both samples revealed similar results. In both sections, pyroxene-pyrrhotite skarn is represented by the coupling of Al, Ca, Fe, Mn and S; these elements are decoupled from Si which represents the cross-cutting quartz vein (Figure 18 and Figure 19). The pyroxenes rims from sample X25 are altered and enriched in Mn relative to cores (Figure 19), likely by the fluids that formed the late quartz veins. Accordingly, late type-ii apatite show a positive correlation between Eu anomalies and Mn content whereas early type-ii apatite show a negative correlation (Figure 20). The Mn enrichment in late type-ii apatite indicate that they are likely associated with this late Mn rich fluid. Images from both samples reveal the coupling of W and Si, representing coarse grained scheelite associated with the quartz vein hosted. These paragenetic associations suggest the first early ore fluid formed prograde skarn assemblages as well as the associated early type-ii apatite. The late fluid, which produced quartz veins and type-iii apatite, may have subsequently altered the wallrock to form retrograde skarn and late type-ii apatite.
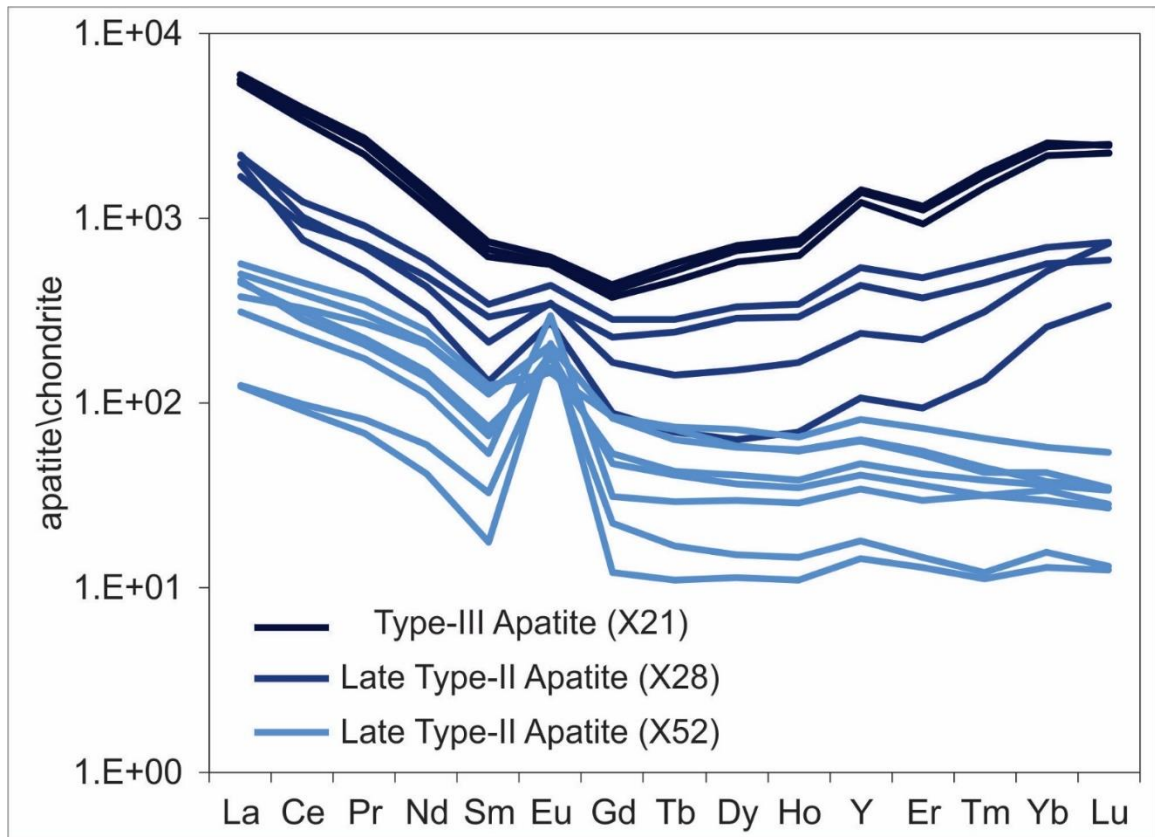
Figure 17: CN REE patterns of late type-ii apatite and type-iii apatite. Apatite show similar MREE depleted CN REE patterns with positive or no Eu anomaly. These CN signatures appear to reflect a continuum between two end member compositions.
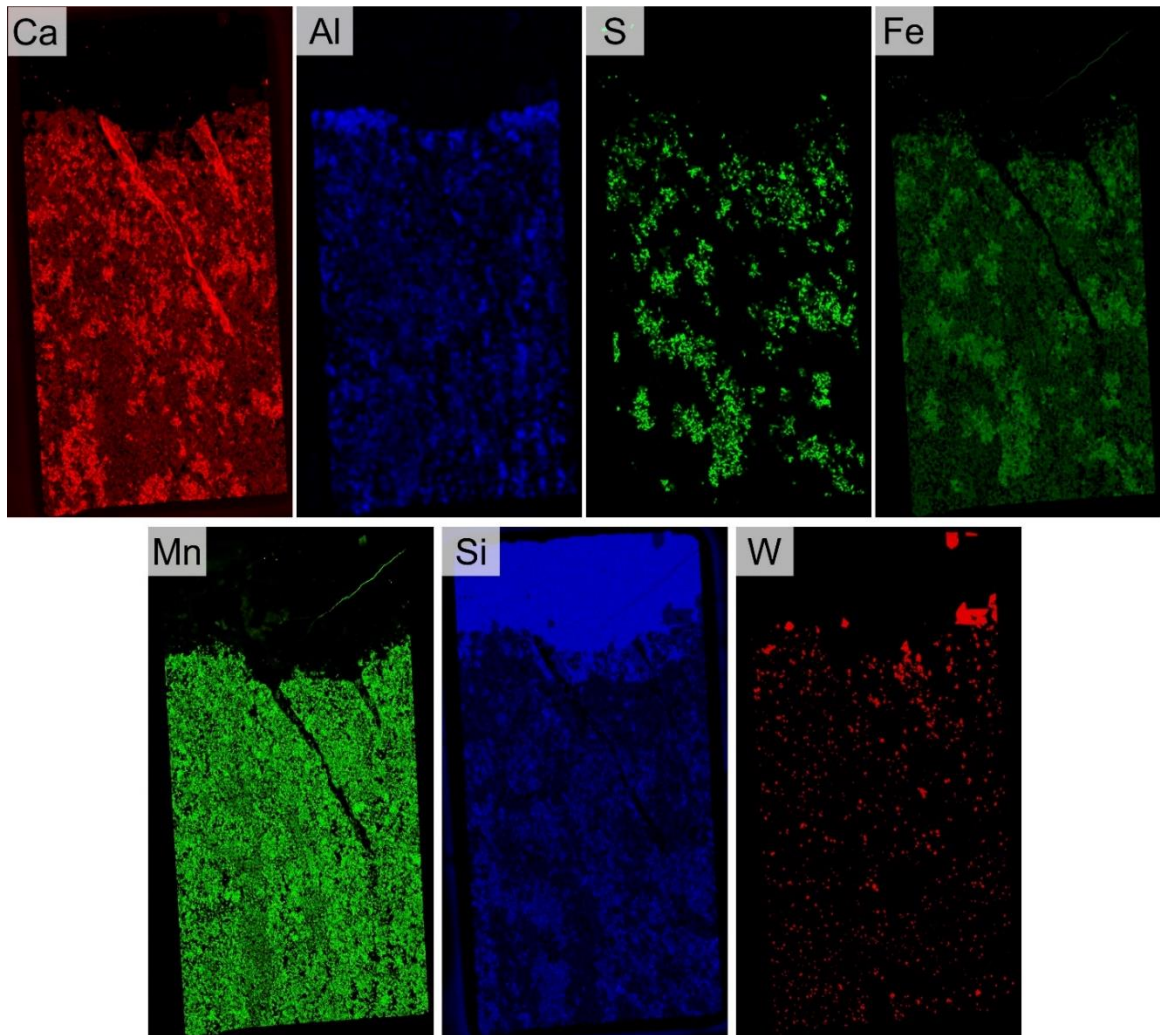
Figure 18: XRF images of sample X21 showing relative elemental abundances of Ca, Al, S, Fe, Mn, Si and W. Prograde pyroxene skarn is represented by the coupling of Ca, Al, S, Fe and Mn. This early assemblage is by crosscut by a late quartz vein (Si) that is associated with coarse grain scheelite mineralization (W).
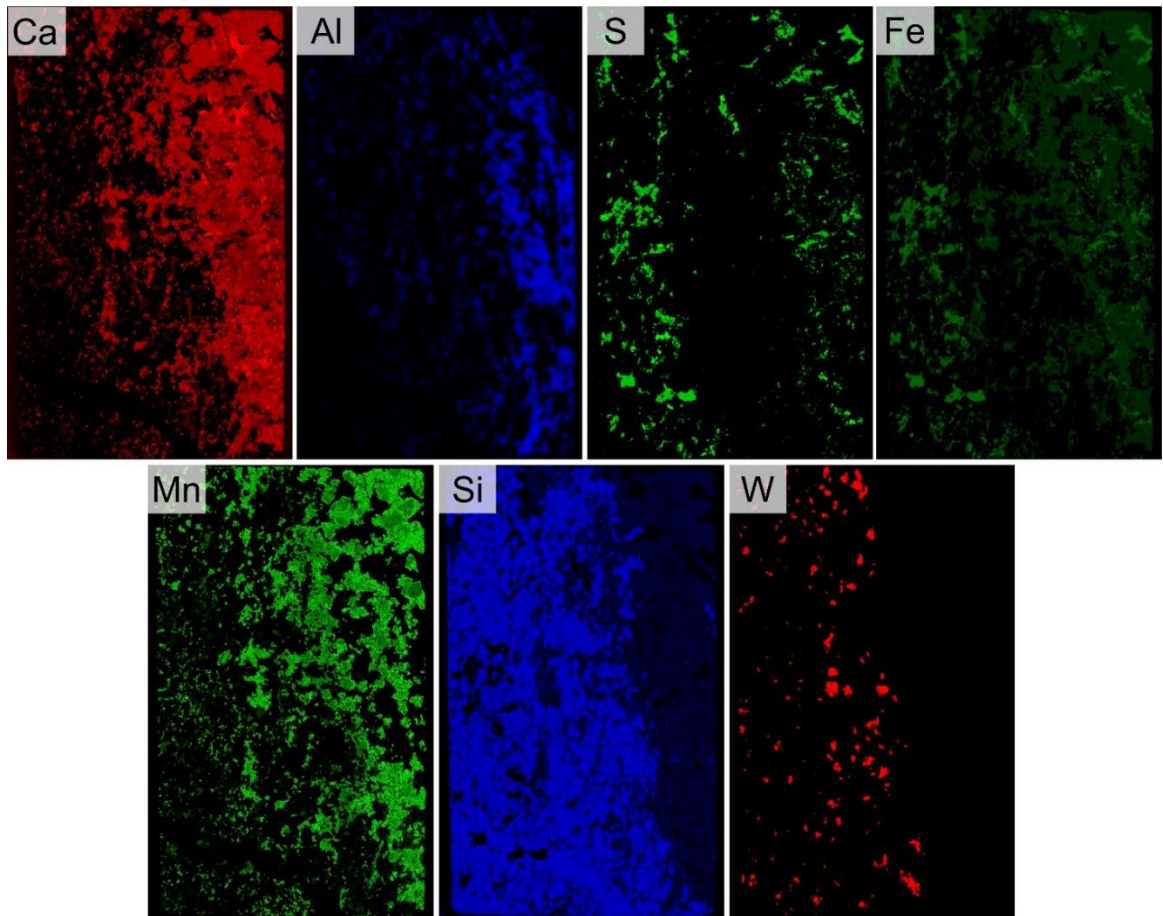
Figure 19: XRF images of sample X25 showing relative elemental abundances of Ca, Al, S, Fe, Mn, Si and W. Prograde pyroxene skarn is represented by the coupling of Ca, Al, S, Fe and Mn. Elemental map of Mn shows altered pyroxene rims which are enriched in Mn relative to core. The early skarn assemblage is by crosscut by a late quartz vein (Si) that is associated with coarse grain scheelite mineralization (W).
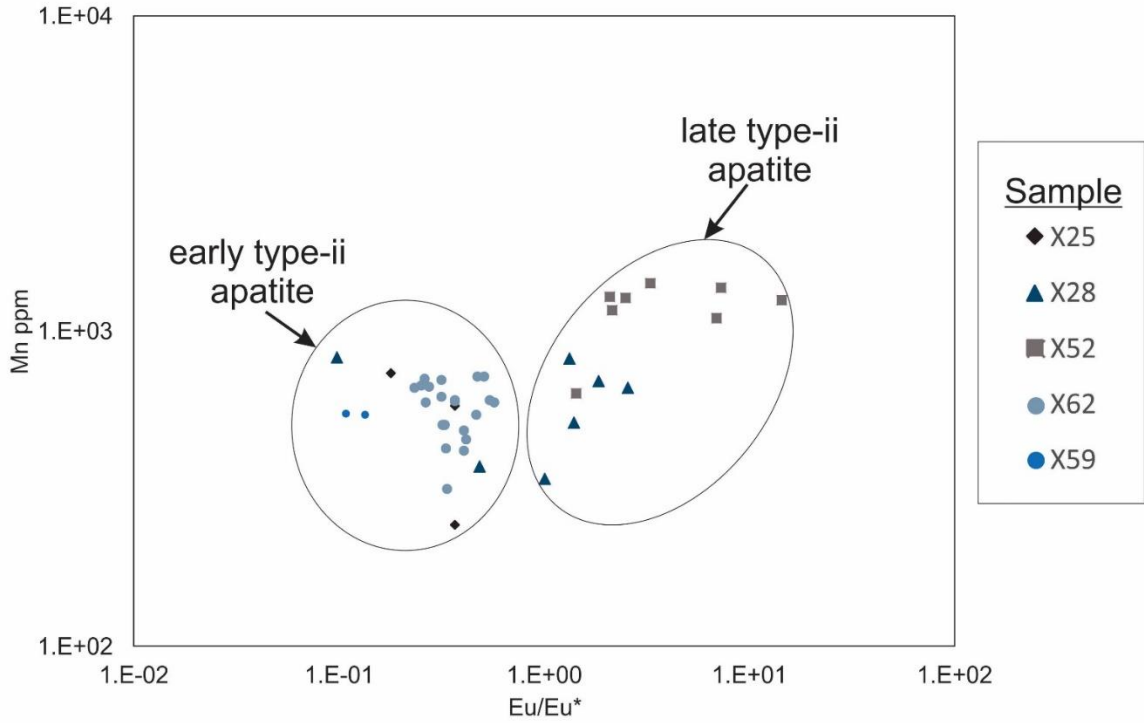
Figure 20: Biplot of Eu anomaly vs. Mn content of type-ii apatite. Early type-ii apatite show no correlation whereas late type-ii apatite show a positive correlation. This trend is consistent with the idea late type-ii apatite are derived from the second Mn enriched fluids.

Model for hydrothermal apatite and evolution of skarn fluids

Considering the paragenesis of type-ii and type-iii apatite, and its association with scheelite mineralization, a two fluid model is proposed. Prograde skarns (i.e. pyroxene) with early type-ii apatite are produced by the first fluid. In accordance with the CN REE signature of early type-ii apatite, the first mineralizing likely had a high flat lying CN REE+Y pattern with a strong negative Eu anomaly (Figure 21).

Retrograde skarn (i.e. amphibole and biotite), as well as quartz veins and coarse-grained scheelite mineralization is produced by the second fluid. Late type-ii and type-iii apatite precipitated from this second fluid and likely reflect its REE chemistry. The REE chemistry of late type-ii and type-iii apatite indicate that the fluid is MREE depleted with a weak positive or no Eu anomaly. Considering the distribution of late type-ii (disseminations in retrograde skarn) and type-iii (euhedral inclusions in quartz veins) apatite, as well as CN REE patterns, type-iii apatite likely precipitates prior to late type-ii apatite. Type-iii apatite crystallizes early in the veins, while late type-ii apatite and forms by fluids that penetrated the wallrock and altered prograde skarn to retrograde skarn and/or enriched pyroxene in Mn. Coarse-grained scheelite forms along fracture margins and the system sealed by late-forming quartz. The CN REE signature of quartz vein hosted type-iii apatite may closely reflect that of the "unfractionated" second fluid. Late type-ii CN REE signatures suggest that crystallization of apatite depleted MREE of the fluid, forming positive Eu anomalies overtime (Figure 21); similar to the mechanism for scheelite and apatite crystallization of the Mt. Charlotte and Drysdale Au deposits in Australia Brugger et al (2000).

Although the REE chemistry and paragenesis of hydrothermal apatite from the Mactung deposit indicate two chemically distinct ore fluids, it remains unclear whether the

REE signatures of apatite reflect fluids originating from a single source or two distinct sources. Fractionation at the source can alter the chemistry of the derived hydrothermal fluids and can therefore justify the observed chemically distinct fluids. The CN REE signature of early type-ii apatite is consistent with fluids associated with felsic magmatism, such fluids commonly have a high REE content, $LREE_N/HREE_N > 1$, and show negative Eu anomalies due to the fractionation of plagioclase in the source magma (Watson & Capobianco, 1981). The late fluid may have been derived from the same felsic source, but subsequent crystallization of magmatic MREE-rich minerals such as apatite, allanite and scheelite, may have generated a chemically distinct late magma and fluid. Alternatively, hydrothermal MREE-rich minerals may have crystallized closer to the fluid source than the location of the sampled area for this study. The Mactung deposit is suggested to form by fluids from a blind intrusion, far below and to the south of the exposed deposit (Selby et al., 2011; Atkinson & Baker, 1986). Early fractionation of MREE by minerals that crystallize closer to the source could produce the chemically distinct fluids. Further investigation of apatite in the area suspected to be closer to the source pluton is required to determine whether there is deposit scale zoning in apatite chemistry.

Conversely, the fluids may be derived from two different sources. As previously mentioned, the CN REE signature of the early fluid (i.e. CN REE of early type-ii apatite) is consistent with a fluids derived from felsic magmatism. The second fluid is characterized by the high $\Sigma REE+Y$, MREE depleted CN REE pattern with no Eu anomaly. The lack of Eu anomaly either indicates that plagioclase was not fractionated at the source (if magmatic) or the fluid was oxidized and Eu^{3+} prevailed. The possible source of the fluid remains unclear at this stage of the study but could be constrained with future research.

Regardless of source, such unique MREE depleted fluids must have been fractionated prior to mineralization of type-ii/iii apatite.
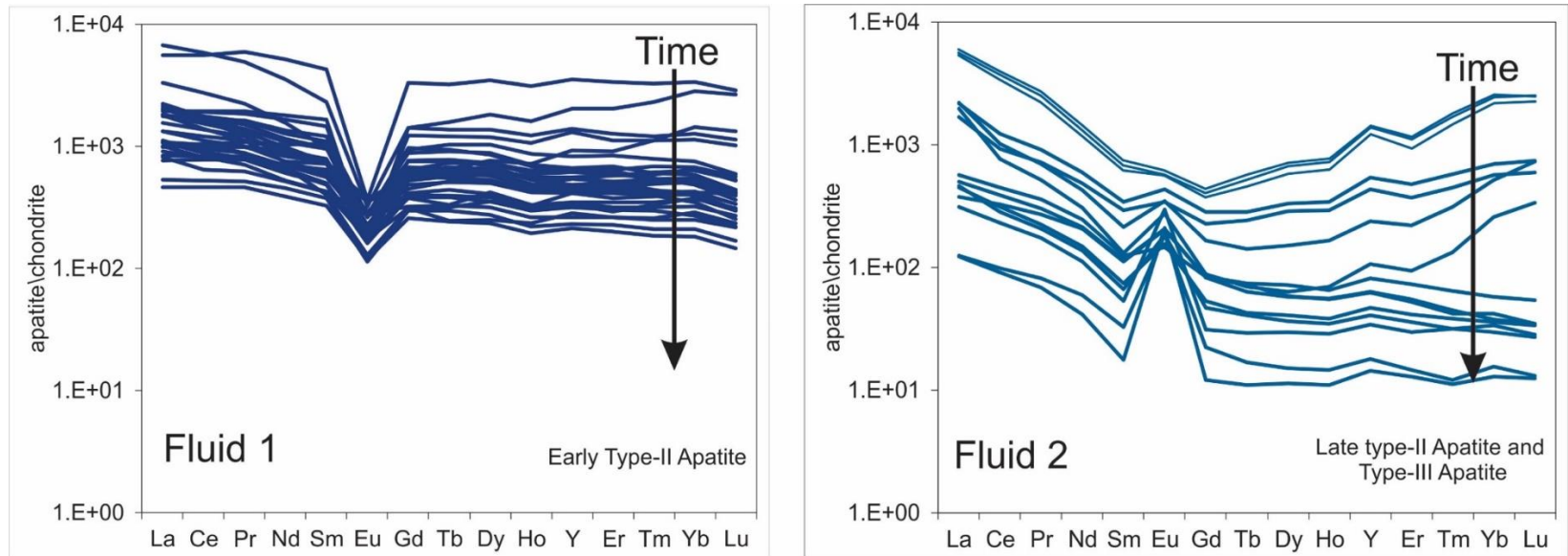
Figure 21: A) All CN REE signatures of early type-ii apatite. The apatite are likely derived from the chemically distinct early fluids associated with prograde skarn formation and therefore likely reflect its REE chemistry and composition. The deposit scale fractionation of REE likely caused the observed decrease in the total REE and Eu anomalies of apatite. B) All CN REE signatures of late type-ii and type-iii apatite. These apatite are likely derived from the chemically distinct second fluid. The variable CN REE signatures of these apatite suggest that fractionation by apatite or other phases depleted REE, particularly MREE and HREE, from the fluid eventually leading to the observed low REE+Y CN REE signatures with depleted MREE and positive Eu anomalies.

Conclusion

The REE chemistry of apatite from the Mactung deposit indicates the occurrence of both non-hydrothermal and hydrothermal apatite. Apatite classified in this study represent three chemically distinct generations of apatite, each of which record distinct moments in the systems evolution. The spatial association and CN REE signature of type-i apatite indicate that they are derived from the recrystallization of associated phosphate nodules. These apatite likely record contact metamorphism of the deposit caused by the intrusion of the ore related pluton. Type-ii and type-iii apatite record the evolution of hydrothermal ore fluids. Considering the REE chemistry of all hydrothermal apatite (i.e. early and late type-ii and type-iii apatite) it appears that two chemically distinct fluids influenced skarn formation and scheelite mineralization at the Mactung deposit. Early type-ii apatite are likely derived from the first fluid and record its chemical composition, these apatite show flat lying CN REE patterns with negative Eu anomalies are consistent with hydrothermal fluids derived from felsic magmatism. The REE chemistry of type-ii and type-iii apatite suggest a second chemically distinct ore fluid. Petrographic evidence indicates that this fluid produced the high grade, coarse-grained scheelite mineralization, along with quartz veins and retrograde skarn. The CN REE of the associated late type-ii and type-iii apatite indicate that the fluid was MREE depleted with no Eu anomaly. At this stage of research it remains unclear whether both fluids are derived from the same source or two different sources. Future work such as the analysis and characterization of the scheelite REE chemistry, a fluid inclusion study, age dating of different apatite generations and an in situ oxygen isotope study are recommended in order to adequately model the evolution of mineralizing fluids at the Mactung W (Cu, Au) skarn deposit. The research conducted through this study does indicate that apatite does have the ability to record the evolution of

fluids in geochemical systems. Different generations of apatite based on petrography, and trace element chemistry reflect distinct moments in the evolution of ore fluids. The results of this study do indicate that apatite has a great potential in furthering the understanding of ore systems and their formation.

Acknowledgements

References

Adlakha, E., Hanley, J., Falck, H., Boucher, B. (2018). The origin of mineralizing hydrothermal fluids recorded in apatite chemistry at the Cantung W-Cu deposit, NWT, Canada. *European Journal of Mineralogy, 30*, 1095-1113

Atkinson, D., and Baker, D. (1986). Recent developments in the geologic understanding of Mactung. *Mineral Deposits of Northern Cordillera. 37,* 234–244.

Ayers, J., and Watson, B. (1993). Apatite/fluid partitioning of rare-earth elements and strontium: Experimental results at 1.0 GPa and 1000°C and application to models of fluid-rock interaction. *Chemical Geology, 110,* 299-314

Bouzari, F., Hart, C., Bissig, T., Barker, S. (2016). Hydrothermal Alteration Revealed by Apatite Luminescence and Chemistry: A Potential Indicator Mineral for Exploring Covered Porphyry Copper Deposits. *Economic Geology, 111,* 1397-1410

Brugger, J., Lahaye, Y., Costa, S., Lambert, D., Bateman, R. (2000). Inhomogeneous distribution of REE in scheelite and dynamics of Archaean hydrothermal systems (Mt. Charlotte and Drysale gold deposits, Western Australia). *Contributions to Mineral Petrology, 139,* 251-264

Dawson, K. (1996). Skarn tungsten. *Geology of Canadian Mineral Deposit Types, 8,* 495-502

Dick, L., and Hodgson, C. (1982). The MacTung W-Cu(Zn) Contact Metasomatic and Related Deposits of the Northeastern Canadian Cordillera. *Economic Geology, 77,* 845-867

Einaudi, M., and Burt, D. (1982). Introduction Terminology, Classification, and Composition of Skarn Deposit. *Economic Geology, 77,* 745-754

Eisbacher, H. (1981). Late Mesozoic-Paleogene Bowser Basin molasse and Cordilleran tectonics, western Canada. *Sedimentation and Tectonics in Alluvial Basins*, *23*, 125-151.

Pan, Y., and Fleet, M. (2002). Compositions of the apatite-group minerals: substitution mechanisms and controlling factors. *Reviews in Mineralogy and Geochemistry*, *48*, 13-49.

Fleet, M., and Pan, Y. (1995). Site preference of rare earth elements in fluorapatite. *American Mineralogist , 80,* 329–335

Gadd, M., Layton-Matthews, D., Peter, J. (2016). Non-hydrothermal origin of apatite in SEDEX mineralization and host rocks Howard's Pass district, Yukon, Canada. *American Mineralogist, 101,* 1061-1071

Genna, D., Gaboury, D., Roy, G. (2014). Evolution of a volcanogenic hydrothermal system recorded by the behavior of LREE and Eu: Case study of the Key Tuffite at Bracemac–McLeod deposits, Matagami, Canada. *Ore Geology Review, 63,* 160-177

Gerstner, M., Bowman, J., Pasteris, J. (1989). Skarn formation at the Macmillan Pass tungsten deposit (Mactung), Yukon and Northwest Territories, I. P-T-X-V characterization of the methane-bearing fluids. *The Canadian Mineralogist, 27,* 545-563

Gromet, L., Haskin, L., Korotev, R., and Dymek, R. (1984). The "North American shale composite": its compilation, major and trace element characteristics. *Geochimica et Cosmochimica Acta*, *48*, 2469-2482.

Harlov, D. (2015). Apatite: A Fingerprint for Metasomatic Processes. *Elements, 11,* 171-176

Hughes, J., and Rakovan, J. (2015). Structurally Robust, Chemically Diverse: Apatite and Apatite Supergroup Minerals. *Elements, 11,* 165–170.

Hughes, J., and Rakovan, J. (2002). The crystal structure of apatite, Ca-5(PO4)(3)(F,OH,Cl). *Reviews in Mineralogy & Geochemistry, 48,* 1-12

Ketcham, R. (2015). Technical Note: Calculation of stoichiometry from EMP dad for apatite and other phases with mixing on monovalent anion sites. *American Mineralogist, 100*, 1620-1623

La Cruz, N., Adam, S., Wolf, A., Martin, R., Fernando, B., Gnagnon, J. (2019). The geochemistry of apatite from the Los Colorados iron oxide-apatite deposit, Chile: implications for ore genesis. *Mineralium Deposita.*

Lang, J., & Baker, T. (2001). Intrusion-related gold systems: the present level of understanding. *Mineralium Deposita*, *36*, 477-489.

Lipin, R., and Mckay, A. (1989). Geochemistry and Mineralogy of Rare Earth Elements. Reviews in Mineralogy, 21, 348

Mair, J., Hart, C., & Stephens, J. (2006). Deformation history of the northwestern Selwyn Basin, Yukon, Canada: Implications for orogen evolution and mid-Cretaceous magmatism. *Geological Society of America Bulletin*, *118*, 304-323.

McArthur, J., Walsh, J. (1985). Rare-Earth Geochemistry of Phosphorites. *Chemical Geology, 47,* 191-220

Meinert, L. (1992). Skarns and skarn deposits. *Geoscience Canada, 19*, 145-162

Selby, D., Hart, C., Heaman, L. (2011). Re-Os and U-Pb geochronology of the Clear Creek, Dublin Gulch, and Mactung deposits, Tombstone Gold Belt, Yukon, Canada: Absolute

timing relationships between plutonism and minerals. *Canadian Journal of Earth Sciences, 40*, 1839-1852

Stock, J., Humphreys, M., Smith, V., Johnson, R., Pyle, D. (2015). New constraints on electron-beam induced halogen migration in apatite. *American Mineralogist*,100, 281–293.

Watson, B., and Green, T. (1981). Apatite/liquid partitioning coefficients for the rare earth elements and strontium. *Earth and Planetary Science Letters, 56,* 405-421

Watson, B., Capobianco, C. (1981). Phosphorus and the rare earth elements in felsic magmas: an assessment of the role of apatite. *Geochimicia et Cosmochimica Acta, 45,* 2349-2358

Webster, J., and Piccoli, P. (2015). Magmatic Apatite: A Powerful, Yet Deceptive, Mineral. *Elements, 11,* 177-182

Appendix

Skarn petrography

Pyroxene-Pyrrhotite Skarn

 Pyroxene-pyrrhotite skarn assemblages contain pyrrhotite (10-20 modal %) and pyroxene (15-25 modal %) as the dominant mineral phases. Other common phases include quartz (5 – 30 modal %) and calcite (5-20 modal %) with lesser plagioclase (1-10 modal %) and trace garnet, vesuvianite and amphibole (Fig. 5a). Pyroxene-pyrrhotite skarn occurs in the 3D and 3E units of the upper ore zone hence, skarn hosted apatite are texturally and spatially associated with phosphate nodules. The paragenetically early phosphate nodules are massive cryptocrystalline aggregates covering 5 - 40 modal % of the assemblage. Type-i apatite occurs in pyroxene-pyrrhotite skarn as anhedral or euhedral grains spatially and texturally associated with phosphate nodules. Small (30 – 350 µm) euhedral apatite and large anhedral apatite are regionally associated with thin crystalline phosphate nodules commonly occurring as inclusions in quartz and pyrrhotite. Apatite contain inclusions of calcite and pyroxene. Pyroxenes occur as small (30 – 750 µm) ubiquitous grains included in quartz and pyrrhotite or sporadically disseminated through phosphate nodules. Scheelite mineralization is likely coeval or sequential to that of pyroxene. Small (150-500 µm) subhedral-euhedral disseminated scheelite have a corroded appearance and are free of inclusions. Large (550 - 1300 µm) anhedral-subhedral scheelite occur with massive quartz flooding or quartz veins. These contain inclusions of pyroxene and plagioclase, related phases include small (85 - 350 µm) euhedral titanite and anhedral pyrrhotite (Fig.). Paragenetically late calcite grains are disseminated anhedral masses interstitial to pyroxene and apatite occasionally overprinting nodules regionally (Fig. 5g and 5e). Pyrrhotite occurs as late crosscutting veins regionally associated with high quartz, scheelite and apatite

mineralization. Late hydrous minerals such as amphibole, clinozoisite and ferro-anthophyllite coat pyroxene and plagioclase phases (Fig. 5i).

Garnet-pyroxene skarn

Garnet-pyroxene skarns contain garnet (15 - 20 modal %) and pyroxene (20 - 25 modal %) as the dominant silicate minerals, accessory minerals include quartz (5 - 25 modal %) and calcite (5 - 10%) with lesser vesuvianite (1 – 5 modal %). Scheelite and pyrrhotite are either absent or present in trace concentrations. Garnet-pyroxene skarn occurs in the 3D and 3F units of the upper ore zone. Lithologies host phosphate nodules which constitute 5-35 modal % of skarn assemblage's . Type-i apatite hosted in garnet-pyroxene skarns occur as either: i) large (500 – 600 µm) euhedral apatite adjacent to a small disseminated phosphate nodule, which contain inclusions of pyroxene and are hosted in pyrrhotite or ii) Garnet hosted anhedral apatite associated with large disseminated nodules, calcite and vesuvianite. Pyroxenes are small (70 – 250 µm) anhedral grains intercalated with anhedral apatite. Pyroxenes are inclusions in garnet, calcite or vesuvianite. Textural evidence suggest that pyroxene mineralizing closely predates that of garnet. Garnets are coarse-grained (150 µm-700µm), polycrystalline aggregates or isometric euhedral crystals. Garnet is optically isotropic too weakly anisotropic, with anisotropic grains displaying occasional zoning observable under cross-polarized light. Vesuvianite are corroded subhedral columnar grains regionally associated with garnet, pyroxene and calcite. Calcite grains are anhedral disseminate masses interstitial to pyroxene and apatite, grains overprint phosphate nodules and vesuvianite locally. Garnet pyroxene skarn do not accommodate scheelite, mineralization only occurs in late crosscutting quartz veins.

Pyroxene Skarn

Pyroxene skarn assemblages comprise abundant quartz (20-35 modal %) and pyroxene (20 – 30 modal %) with lesser calcite (5-10 modal %), plagioclase (2 – 10 modal %), pyrrhotite (<5 modal %), apatite (1-5 modal %), titanite (<2 modal %), amphibole (<2 modal %) and scheelite (5-7 modal %). Pyroxene skarns occurs in the 3D, 3C and 2B units. Phosphate nodules are not observed in individual samples. Apatite occurring in these skarn are classified as early and late type-ii apatite based on their REE chemistry. Apatite grains are paragenetically early with various habits, abundances and size. Trace concentrations of small (75 - 150 µm) prismatic apatite occur as inclusions in scheelite and quartz (Samples X57, X45 and X25). Low abundances (2 – 3 modal %) of large (100 - 350 µm) prismatic apatite are locally concentrated occurring as inclusions in late pyrrhotite, pyroxene, scheelite and quartz. Abundant (5 modal %) large (100 µm- 1.65 mm) subhedral apatite regionally concentrate in quartz, these apatite contain inclusions of monazite and magnetite. Early small subhedral pyroxenes are coated and partially replaced late amphibole, early pyroxene supersedes apatite and is likely coeval to titanite. Large (450 µm - 3.3 mm) titanite are euhedral grains hosted in late quartz, EDS analyses reveal the presence of ilmenite and apatite inclusions. Scheelite mineralization appears to closely supersede that of titanite and pyroxene. Scheelite are large (450 µm - 3.3 mm) subhedral or euhedral grains bearing inclusions of apatite and early pyroxene. The highest scheelite grades occur in pyroxene skarn with modal abundances ranging for 5 - 7 modal %. These aforementioned scheelite, titanite and apatite occur together regionally. Small (33 µm – 66 µm) anhedral plagioclase are disseminated corroded grains intercalated with clinozoisite. Paragenetically late large (500 µm - 3.3 mm) euhedral pyroxene grains with perfect cleavage supersede plagioclase

formation, grains are extensively replaced by late hydrous phases (clinozoisite, amphibole and prehnite) along grains boundaries and contain inclusions of apatite, early pyroxene, titanite and scheelite.

Pyrrhotite skarn

Pyrrhotite skarn assemblages host abundant pyrrhotite (30 - 50 modal %), quartz (15 - 20 modal %) and plagioclase (7 - 10 modal %) with variable pyroxene (5 – 15 modal %) and amphibole (2 – 10 modal %). Chalcopyrite, calcite, titanite and pentlandite occur in trace concentrations. Skarns are restricted to the lower ore zone (2B unit), phosphate nodules occur in all sections (samples X36 and X52). Both type-i apatite and type-ii apatite occur in pyrrhotite skarn. Type one apatite are large (650 - 1300 µm) euhedral crystals adjacent to phosphate nodules (sample X36) or large (300 - 350 µm) anhedral apatite neighboring nodules (sample X52). Type-i apatite from sample X36 contain inclusions of pyroxene indicating that it is paragenetically late, bismuth occurrences are detected along grain boundaries (Fig. 3g). Type-ii apatite (sample X52) are small euhedral disseminated grains hosted in pyrrhotite or late quartz. Such apatite are highly abundant comprising approximately >10 modal % of the assemblage. Pyroxenes are small anhedral disseminate grains occurring as inclusions in quartz, grains are extensive replaced by amphibole. Scheelite occurs in trace concentrations as small anhedral grains with a corroded appearance. Plagioclase forms acicular ubiquitous crystal hosted in pyrrhotite or quartz. Pyrrhotite skarn host large amphibole laths formed through the extensive replacement of pyroxenes (Fig. 8g). Late quartz grains are disseminated through pyrrhotite, hosting abundant apatite, pyroxene and plagioclase inclusions.

Biotite skarn

Biotite skarns are a rare assemblages accommodating abundant biotite (15-20 modal %), amphibole (5-15 modal %), pyrrhotite (15-25 modal %) and quartz (25-30 modal %) with trace muscovite and chalcopyrite. Biotite skarns only occurs in 2B unit (sample X29) and 3C units (X28 and X46). Phosphate nodules are always absent. Only late type-ii apatite occurs in these skarns. Apatite are paragenetically early small euhedral disseminated grains largely occurring as inclusions in quartz, pyrrhotite and scheelite. Monazite inclusions in apatite are detected via EDS. Scheelite are small (65-250µm) disseminated inclusions in quartz and pyrrhotite, grains are euhedral and free of inclusions, this characteristic is only observed in these skarns. Small (25 - 150 µm) subhedral biotite form laths or rounded grains hosted in quartz. Amphiboles occurs large green laths commonly altered and replaced by biotite. The replacement of amphibole by biotite is observed in all samples, although the degree of replacement is variable.

Wollastonite skarn

Wollastonite skarn assemblages host abundant wollastonite (>20 modal%), quartz (10-25 modal %), plagioclase(5-15%), calcite (2-10%), clinozoisite (5-7%) and pyroxene (2-5%). Wollastonite skarn is observed in two samples (X2 and X18) from the 3F and 3D units respectively. Phosphate nodules and acicular apatite are paragenetically early occurring in both 3D and 3F skarn. Trace scheelite (<1 modal %) are small (0.170-330 µm) decimated anhedral crystals, scheelite mineralization supersedes that of apatite, an is either coeval or sequential to that of pyroxene. Early small (50-100 µm) pyroxene are subhedral tabular grains occurring in trace concentrations. Wollastonite are small (50-70 µm) anhedral disseminated grains, occurring with paragenetically late small (50-100 µm)

tabular or needle-like plagioclase. Plagioclase coats wollastonite, with grain textures indicating a disequilibrium between the two phases. Trace pyrrhotite are late disseminated anhedral grains. Fine grained acicular clinozoisite are ubiquitous occurring with plagioclase. In the 3D unit wollastonite skarn assemblages (Sample X18) are crosscut by a late vein bearing large euhedral quartz, garnet, vesuvianite and fluorite. Early garnet is regionally overprinted by late disseminated fluorite, both phases occur locally as large crystal aggregates.

Mineral composition

Garnet

Chemical composition of garnet hosted in garnet-pyroxene skarn (X50, X53, X9, X58) and pyroxene-pyrrhotite skarn (X49 and X27) was quantified via 38 EDS analyses (Table 2). Garnet contains high variable CaO (22.63-34.04 wt%), Al_2O_3 (15.68-20.92 wt%) and SiO_2 (39.36-43.17 wt%) with moderate FeO_t (3.55-12.03 wt%) and variably low TiO_2 (<1.72 wt%), MnO (<5.56 wt%) and MgO (<1.59). Trace F (2.24- 4.09 wt%) is detect in select samples (X53, X49, X27, X9). Garnet from garnet-pyroxene skarn sample X50 exhibits the widest range in composition with variable low CaO (22.63-33.48 wt%) coupled with high FeO_t (5.51-12.03 wt%) and MnO (1.59-5.56 wt%). Minor concentrations of V_2O_5 (<054 wt%) are also present in garnet from this sample. Garnet from sample X9 contains essentially no Mg or Mn. All samples contain garnet with quantifiable amounts of Ti with the highest Ti concentrations occurring in garnet from samples X27, X49 and X9.

The data in wt% oxide were recalculated to atoms per formula unit based on 12 oxygen (Table 3) and the general formula $X_3Y_2(SiO_4)_3$, in order to evaluate the garnet speciation and degree of solid solution. Average Atomic formal of garnet hosted in the Mactung is $Ca_{(2.40\pm0.25)}(Al_{(1.73\pm0.09)}Fe_{(0.40\pm0.13)}Mn_{(0.09\pm0.10)}Mg_{(0.02\pm0.04)})(Si_{(3.17\pm0.03)}O_4)_3$.

Calculations were conducted with the assumption that al Fe is Fe^{2+}. This assumption is justified by the presence of abundant pyrrhotite without magnetite, indicating reducing conditions. Based on high Al (1.73±0.09 apfu), the garnet are classified as solid solutions within the pyralspite group (pyrope-almandine-spessartine solid solution) and grossular of the grandite group (grossular-andradite-hydrogrossular solid solution). High Ca (3.17±0.03 apfu) indicates a predominantly grossular component . Acquired data indicates that solid solution dominantly occurs between Ca, Fe and Mn+Mg while the Al content remains consistent. Thus, garnet in the Mactung are a solid solution of grossular, almandine and spessartine+pyrope. These are dominantly Ca rich (i.e. grossularitic) in composition, all grains have Fe and Mn/Mg substitution (fig).

Pyroxene

Chemical composition of pyroxene occurring in the Mactung deposit was quantified through 116 SEM-EDS analyses, average oxides are presented in table 4. Pyroxene have high CaO (21.65±0.60 wt%) with high variable concentrations of FeO_t (17.35±4 wt%) and MgO (5.45±3.43 wt%) coupled with low MnO (1.84±0.72 wt%) and trace Al_2O_3 (<2.19 wt%). Samples X25, X53 and X46 exhibit the widest range in composition. Pyroxenes from sample X25 occur as paragenetically early small subhedral grains or paragenetically late euhedral grains, these accommodate high variable MgO (9.63 ± 2.68 wt %) and FeO_t (12.36 ± 4.17 wt %) with low MnO (1.44±0.58 wt%). Garnet-pyroxene skarn hosted pyroxene from sample X53 encompass high variable MgO (6.35±3.37 wt%) and FeO (16.33±4.18 wt%) coupled with low MnO (1.21±0.46). Amphibole skarn hosted pyroxene from sample X46 have high variable MgO content (13.14±3.50 wt%), high FeO_t (0.10.12±1.14 wt%) and low MnO (1.34±1.14 wt%). Low concentrations of Al_2O_3

(0.49±0.69 wt%) and V_2O_5 (0.04±0.05 wt%) coupled with low variable CaO (18.01±4.61) and high SiO_2 (57.05±1.59 wt%) are exclusive to pyroxenes from sample X46.

Oxide composition of skarn hosted clinopyroxenes were recalculated to atoms per formula unit based on 6 and the general mineral formula XYT_2O_6. The general mineral formula of pyroxenes hosted in the Mactung deposit is $(Fe_{(0.52\pm0.15)} Mg_{(0.29\pm0.17)} Mn_{(0.06\pm0.02)})$ $Ca_{(0.64\pm0.02)} (Si_{(1.92\pm0.03)} O_6)$. In accordance with garnet mineral formula recalculations all Fe is assumed to be Fe^{2+} due to high pyrrhotite content of skarns signifying reducing conditions. Due to the high variable content of Fe and Mg pyroxenes are classified as a solid solution the Calcic pyroxene. Primary substitutions is between Fe (hedenburgite) and Mg (diopside) end members paired with minor Mn (johannsenite) substitution, high Fe (0.52±0.15 apfu) indicates a predominantly Hedenburgitic component (Fig.). Pyroxenes from sample X23 encompass the highest diopside component (0.610±0.098 apfu) while the highest hedenburgite component (0.691±0.070 apfu) occurs in pyroxenes from sample X52, and the highest Johannsenite component (0.079±0.018 apfu) occur in sample X27. Average mineral formulas of skarn hosted pyroxenes are presented in table 5.

Titanite

Analysis of 11 titanite grains from six sections (X18, X28, X63, X25, X45, X46) were acquire. Titanite is paragenetically early phases phase occurring in trace concentrations (Table 6). Large euhedral titanite occur regionally with type two apatite, while small subhedral disseminated grains are pervasive. Titanite contain high variable concentrations of TiO (average= 29.82±4.4) with consistent high CaO (27.01±1.36 wt%) and SiO (33.96±0.94 wt%). Analysed grains contain low variable concentration of FeO (0.99±0.54 wt%) and AlO (5.78±2.80). Modest variable concentrations of F (3.63±1. 90) occurs in

titanite from all samples, F is not detected in select grains from section X45 and X28. Trace concentrations of NbO (0.16±0.50), MnO (0.05±0.15) and NaO (0.12±0.36) are detected in section X28. Chemical composition of titanite does not appear to correlate with variations in habit.